EarthArXiv preprint (Under Review in Remote Sensing of Environment)

Decoding the Dynamics of Climate Change Impact: Temporal Patterns of Surface Warming and Melting on the Nivlisen Ice Shelf, Dronning Maud Land, East Antarctica

Geetha Priya M [a, *], Raghavendra K R [a], Mahesh B [a], Rakshita C [a], Dhanush S [a], Sivaranjani S [a], Deva Jefflin A R [a], Krishna Venkatesh [a], Narendra Kumar M [a], Alvarinho J. Luis [b]

[a] Centre for Incubation Innovation Research and Consultancy (CIIRC), Jyothy Institute of Technology, Bengaluru 560082, Karnataka, India
[b] National Centre for Polar and Ocean Research, Ministry of Earth Sciences, Vasco-da-Gama, Goa 403 804, India
*Corresponding author: geetha.sri82@gmail.com

Abstract. Surface melting in Antarctica can result in the formation of meltwater ponds and streams, which can encourage glacier basal sliding and ice flow; long-term severe surface melting can result in the formation of melt ponds and, eventually, supraglacial lakes (SGLs), raising the prospect of hydrofracturing. Measurements of these surface melting characteristics are useful for studying glacier and ice sheet dynamics and monitoring polar climate change. This work addresses a technical analysis of the dynamics of the Nivlisen ice shelf, East Antarctica, with a focus on multiple components such as melt ponds and SGL parameters (such as area, length, volume, and depth), seasonal surface melt extent, and surface ice flow velocity. For the austral summers of 2000-2023, data from the Landsat and Sentinel-1 have been used to analyze at both spatial and temporal scales. The overall area of melt ponds and SGLs remained relatively low (one square kilometers) during November and December from 2000 to 2014. For the austral summers of 2015-2023, a consistent melting pattern with increased formation of melt ponds and SGLs has been observed. Among the analyzed years, 2016, 2017, 2019, and 2020 have the greatest SGL depth. Maximum volume with progressive growth in the area in SGL was observed during 2008, 2016, and 2020. Understanding the relationship between velocity and basal melt is necessary to comprehend the dynamics of the ice shelf in terms of ice shelf stability and assess the influence of surface melt on seasonal ice velocity patterns. The data analysis showed that January had the most substantial melting, resulting in more significant velocity values. During 2000-2023, surface melt occurred in the southern and northwestern regions of the Nivlisen ice shelf. Our results emphasize the critical role of surface melt in driving ice shelf velocity. The results were validated using ground truth data collected over a melt pond in central Dronning Maud Land during the austral summer of 2022-2023 and verified with model-based results. The increase in depth and volume could significantly impact the integrity of the region's ice shelf. Surface melting conditions that are persistent and obvious will increase the formation of melt ponds and SGL, which accelerates

ice flow and cause ice shelf destabilization. Continuous monitoring of the Antarctic shelves are necessary to access the impact of climate change.

Keywords: Surface Melt, Melt Pond, Ice flow velocity, UAV, Pressure sensor, Antarctica, Landsat, Sentinel-1

1. Introduction

Ice shelves are important features in the Polar Regions, especially in Antarctica, where they regulate the ice flow from the continent to the ocean. However, as a result of major surface melting on the Antarctic ice shelves brought on by climate change, there is a greater loss of ice (Bell et al. 2017)(Dell et al. 2020). Increased ice melting and loss are being caused by rising temperatures and changing precipitation patterns (Arthur, C.R. Stokes, et al. 2020). The preservation of efficient subglacial drainage mechanisms is a major concern as it affects the uninterrupted ice flow and calving of ice shelves (Tuckett et al. 2021)(Sneed and Hamilton 2007)(Stevens et al. 2015). Recent measurements suggest that surface melting is increasing across the Antarctic continent (Husman et al. 2022)(Luis et al. 2022)(Saunderson et al. 2022)(Valerio et al. 2022). These changes in the Antarctic environment impact the meridional temperature gradient, sea level rise, changes in atmospheric conditions, ocean biogeochemical dynamics, and other factors (Rintoul 2018). Understanding the consequences of melting on ice shelves is a major research field for a better understanding of Antarctica's contribution to the rise in the sea level (Geetha Priya et al. 2022) (Jakobs et al. 2020)(Baumhoer et al. 2018)(Ghiz et al. 2021). Surface albedo or reflectivity, as well as weather patterns like heat waves and extreme weather events, have a substantial impact on the amount of surface melt, which varies significantly from year to year (Mortimer et al. 2016) (Hall et al. 2009) (Saunderson et al. 2022).

Minor changes in ice shelves have the potential to have significant effects on global sea level rise and climate patterns (Husman et al. 2022). Surface melting that is prolonged and strong can produce melt ponds and supraglacial lakes (SGL), contributing to ice shelves' instability (Liang et al. 2021)(Colosio et al. 2021)(König and Oppelt 2020). Snow and ice melt enable hydrological features like melt ponds and SGL to form on the surface of glaciers, ice shelves, and ice sheets (Sergienko 2022). They are characterized by the buildup of meltwater in depressions, which over time results in the formation of SGLs (Dell et al. 2022)(Moussavi et al. 2020). Although melt ponds and SGLs are transient in nature, they exhibit significant variability in terms of size, depth, and spatial distribution. Some SGLs can span several kilometers in length and breadth, reaching depths of several meters. By examining variations in the volume and area of circular or linear surface water bodies, meltwater dynamics can be better understood. (Dell et al. 2020). SGLs typically go through a cycle of formation and drainage regularly, with most lakes reabsorbing or emptying during austral summer. (Hawes et al. 2011). However, some SGLs drain, with water seeping through crevasses, moulins, melt channels, or other drainage features potentially influencing the underlying dynamics of the ice (Leppäranta et al. 2020) (Dell et al. 2020)(Sneed and Hamilton 2007)(Liu et al. 2022).

The presence of melt ponds and SGLs reduces the surface reflectivity, or albedo, of glaciers, increasing the amount of solar energy absorbed and enhancing surface melting. (Lombardi et al. 2019)(Jakobs et al. 2021). This, in turn, contributes to the destabilization of ice shelves by warming the surrounding ice column (Furfaro et al. 2014)(Fricker et al. 2021). Lake size, depth, distribution, and atmospheric variables, including temperature and radiation, all play a complex role in the link between SGL development, surface albedo, and ice shelf dynamics. (Arthur, C. Stokes, et al. 2020) (Buzzard et al. 2018). The presence and behavior of SGLs on ice shelves have significant implications for ice shelf stability, including their buttressing impact on inland ice flow (Arthur, C. Stokes, et al. 2020)(Arthur et al. 2022)(Liu et al. 2022).

SGLs in Antarctica may form by a variety of mechanisms, such as the buildup of meltwater on the surface of ice sheets or glaciers, which causes ponds or lakes to develop. Since these water bodies have a lower albedo than the surrounding ice, more solar radiation is absorbed, accelerating surface melting (Arthur, C. Stokes, et al. 2020)(Luis et al. 2022)(Jakobs et al. 2020)(Halas et al. 2023)(Hall et al. 2009)(Lampkin and Karmoskay 2009)(Alley 2017). This localized increase in surface melting contributes to greater meltwater production and expansion of the lakes (Mahagaonkar, A et al. 2023)(Dirscherl et al. 2020). By promoting the flow of meltwater to the ice shelf's base, which causes the ice shelf to melt more quickly and lose some of its structural integrity, the existence of glacial lakes can also make it easier for the ice shelf to collapse (Izeboud and Lhermitte 2023). The interaction between SGLs, surface albedo, and ice shelf dynamics plays a crucial role in understanding the behavior and stability of ice shelves in response to changing environmental conditions (Gardner and Sharp 2010).

In the scientific literature, passive microwave measurements have been widely used to assess the extent and duration of surface melt across the entire Antarctic ice sheet and to investigate trends, teleconnections with the climate, and specific melt episodes (Saunderson et al. 2022) (Cavalieri and Parkinson 2008) (Zhu et al. 2021)(Colosio et al. 2021)(Ghiz et al. 2021)(Steiner and Tedesco 2014)(Trusel et al. 2012)(Oza et al. 2011)(Brogioni et al. 2023)(Johnson et al. 2020). Satellite-based microwave observations have played a crucial role in processing data sources for monitoring surface melt in Antarctica (Liang et al. 2021)(Oza et al. 2011)(Liu et al. 2006)(Ghiz et al. 2021). To assess the depth, size, and amount of meltwater on the Nivlisen ice shelf (NIS), optical data sets have also been used (Dell et al. 2020). Another investigation by Arthur, C. Stokes, et al. (2020) examined the geographic distribution, depth, area, and volume of SGLs on an ice shelf in East Antarctica over a two-decade period and for several melt seasons.

In the present study, microwave Synthetic Aperture Radar (SAR) and optical data were utilized to estimate various parameters of the NIS on the east coast of Antarctica. These parameters include surface melt extent, SGL characteristics (depth, area, and volume), and surface ice flow velocity. The detection of SGL and volumes using satellite optical data is susceptible to underestimating the true extent of meltwater because of restricted availability of cloud-free optical imagery (Tuckett et al. 2021). To validate the estimated pond depth obtained from unmanned aerial vehicle (UAV) multispectral data in this particular experiment, data from a Pressure Sensor Assembly (PSA) installed above a melt pond were employed. The findings of this research provide valuable insights into the vulnerability of the NIS to climate change. They contribute to our understanding of surface melting, melt ponds and SGLs, and the increasing meltwater, thereby providing future predictions related to sea level rise(Pina and Vieira 2022)(Qiao et al. 2023).

The objective of this study is to conduct a comprehensive technical analysis of the dynamics of NIS in East Antarctica. The investigation focuses on multiple components, including SGLs, seasonal surface melt extent, and surface ice flow velocity. The analysis will be conducted at both spatial and temporal scales using satellite data from the Landsat and Sentinel-1 datasets (Alimasi et al. 2020)(Kaushik et al. 2022). The primary goals are to estimate the surface melt extent, determine various parameters related to SGLs (such as area, length, volume, and depth), analyze ice shelf velocity, and assess the influence of surface melt on seasonal ice velocity patterns. In order to validate the results, field measurements have been conducted using pressure sensors to monitor meltwater levels, providing empirical verification.

2. Study Area

Antarctica, one of the world's most extensive ice sheets, spans approximately 98% of the Antarctic region's landmass. Dronning Maud Land is a significant territory in East Antarctica covering more than 2.7 million square kilometres. Its coastline stretches for approximately 2,000 kilometres, and massive ice shelves are a notable feature. A crucial factor in determining the amount of melt on the ice shelf's surface is surface ice loss (Arthur, C. Stokes, et al. 2020)(Vaňková et al. 2021)(Bell et al. 2018)(Ghiz et al. 2021)(Husman et al. 2022)(Alley 2017). NIS was chosen for this study since there has been a recent increase in melt ponds and SGLs over the ice shelf region, and it is undergoing significant melting throughout the austral summer, leading to the formation of SGLs. This occurrence makes the ice shelf more vulnerable to hydrofracturing (Cook and Vaughan 2010)(Jakobs et al. 2020)(Aoki et al. 2017)(Baumhoer et al. 2018)(Kingslake et al. 2017)(Liang et al. 2021)(Trusel et al. 2022), making it a vital area for studying the processes and causes that lead to ice loss on the Antarctic ice shelf (Trusel et al. 2012).

As illustrated in Fig 1, NIS has an extent of around 7600 square kilometers and extends roughly 80 kilometres north-south and 130 kilometres east-west into the Lazarev Sea (Dell et al. 2020). With ice thickness ranging from 150 to 700 metres, the NIS (70.3S, 11.3E) is situated in the centre of Dronning Maud Land (cDML) between the Vigrid and Lazarev ice shelves (Horwath et al. 2006)(Mahagaonkar, A et al. 2023). Potsdam Glacier feeds NIS from the southeast, with an average ice thickness of 1000 m. The bare ice in the southeast corner of the ice shelf moves at an average speed of 80 my^{-1} due to the katabatic winds. The Schirmacher Oasis, a region free of ice with a maximum elevation of 250 metres above sea level and a lot of lakes and ponds, is situated in the southern part of NIS (Lindbäck et al. 2019). Summer surface melting creates melt ponds and SGLs, exposing Nivlisen to hydrofracturing. Melt pond and SGL are observed on the north, west and southern regions of NIS. Since 2016, meltwater ponding has evolved due to the temperature rise. NIS is melting rapidly, making it a strategic location for investigating the dynamics and influencing factors of ice loss on the Antarctic ice shelf (Alley et al. 2018). The outcomes of this study will be used to make future predictions of sea level rise in terms of surface melt, SGL, and meltwater rise and to analyse the NIS's vulnerability to climate change.

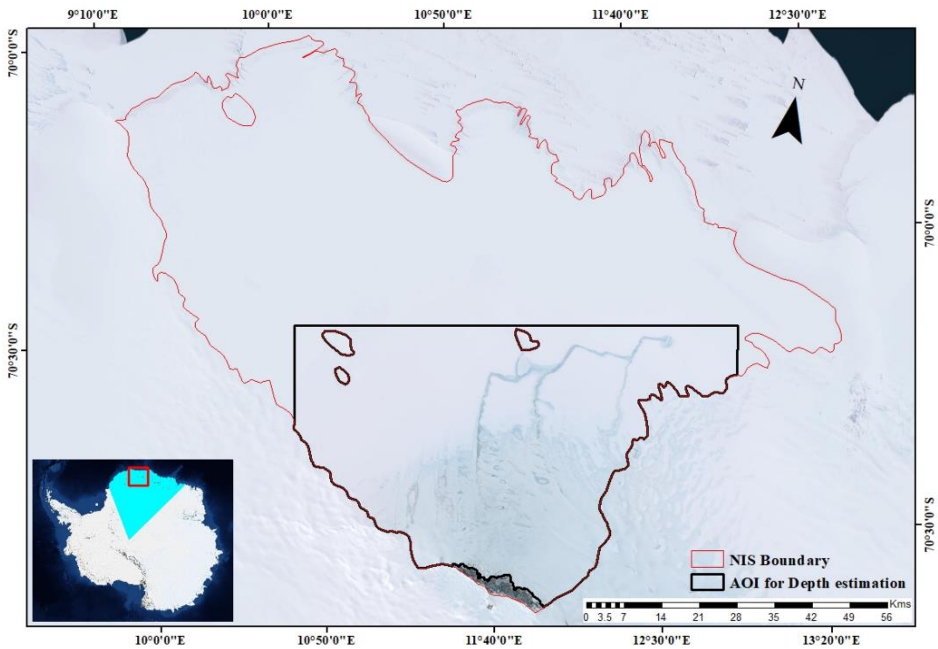

Fig. 1. Study area on East Antarctica consisting of Nivlisen Ice Shelf, central Dronning Maud Land located at 70.3 °S,11.3°E with a 2000 km coastline encompassing large ice shelves with the coordinate reference system “WGS84 Antarctic polar stereographic.”

3. Data

For estimating the seasonal variations in the geometry of melt ponds and SGLs, satellite-based multispectral datasets were employed. The data were compiled using the USGS Earth Explorer platform, specifically utilizing the Landsat-7, Landsat-8, and Landsat-9 satellites, during the austral summer (from November to February) of 2000-2023 with minimal or no cloud cover. Landsat-7 was launched on April 15, 1999, and is equipped with the Enhanced Thematic Mapper Plus (ETM+) sensor, featuring eight spectral bands and a spatial resolution of 15-30 m (Tuckett et al. 2021). Landsat-8, launched on February 11, 2013, includes the Operational Land Imager (OLI) and the Thermal Infrared Sensor (TIRS) (Moussavi et al. 2020). It offers 11 spectral bands, a swath size of 185 x 180 km, and a spatial resolution ranging from 15 to 100 m. Landsat-9, which shares the same capabilities and resolution as Landsat-8, was launched on September 27, 2021 (Masek et al. 2020). Table 1 presents the specific data used (path 165-166 and row 110) and due to cloud cover, there were data gaps for the years 2002, 2004, 2005, 2006, 2009, and 2013.

The study utilizes Synthetic Aperture Radar (SAR) data, which enables data collection in all weather conditions and during the day or night. The SAR data was searched and downloaded from the Alaska Satellite Facility (ASF) website (https://search.asf.alaska.edu/). For surface melt and surface velocity estimations, the study makes use of Sentinel-1 microwave SAR data, which is part of the Copernicus Earth monitoring program launched by the European Space Agency (ESA)(Liang et al. 2021)(Manickam et al. 2017). The Sentinel-1 mission consists of two polar-orbiting satellites, Sentinel-1A, and Sentinel-1B, launched in 2014 and 2016, respectively. These satellites provide a revisit period of 6 days (Barella et al. 2022). Equipped with C-band SAR instruments operating at a frequency of 5.4 GHz, they capture high-resolution images of the Earth's surface.

Table 1 Data used for estimating the Depth of Melt Ponds and SGLs for the Austral summer (NDJF) of the years 2000-2023

Serial No.	Scene ID	Date of acquisition
1.	LE07_L1GT_166110_20000106_20200918_02_T2	06/01/2000
2.	LE07_L1GT_165110_20010101_20200917_02_T2	01/01/2001
3.	LE07_L1GT_166110_20030114_20200916_02_T2	14/01/2003
4.	LE07_L1GT_165110_20070118_20200913_02_T2	18/01/2007
5.	LE07_L1GT_165110_20080105_20200913_02_T2	05/01/2008
6.	LE07_L1GT_165110_20100126_20200911_02_T2	27/11/2010
7.	LE07_L1GT_166110_20110205_20200910_02_T2	13/12/2011
8.	LE07_L1GT_165110_20120201_20200909_02_T2	02/02/2012
9.	LC08_L1GT_165110_20140214_20201016_02_T2	14/02/2014
10.	LC08_L1GT_166110_20151123_20201016_02_T2	23/11/2015
11.	LC08_L1GT_166110_20151209_20201016_02_T2	09/12/2015
12.	LC08_L1GT_166110_20160126_20201016_02_T2	26/01/2016
13.	LC08_L1GT_166110_20160126_20201016_02_T2	11/02/2016
14.	LC08_L1GT_165110_20161102_20201016_02_T2	02/11/2016
15.	LC08_L1GT_166110_20161227_20201016_02_T2	27/12/2016
16.	LC08_L1GT_165110_20170105_20201016_02_T2	05/01/2017
17.	LC08_L1GT_166110_20170213_20201016_02_T2	13/02/2017
18.	LC08_L1GT_167110_20171103_20201016_02_T2	03/11/2017
19.	LC08_L1GT_167110_20171221_20201016_02_T2	21/12/2017
20.	LC08_L1GT_167110_20180207_20201016_02_T2	07/02/2018
21.	LC08_L1GT_165110_20181108_20201016_02_T2	08/11/2018
22.	LC08_L1GT_166110_20181201_20201016_02_T2	01/12/2018
23.	LC08_L1GT_167110_20190125_20201016_02_T2	25/01/2019

24.	LC08_L1GT_166110_20190219_20201016_02_T2	19/02/2019
25.	LC08_L1GT_165110_20191213_20201023_02_T2	13/12/2019
26.	LC08_L1GT_165110_20200114_20201016_02_T2	14/01/2020
27.	LC08_L1GT_165110_20201129_20210316_02_T2	29/11/2020
28.	LC08_L1GT_166110_20201222_20210310_02_T2	22/12/2020
29.	LC08_L1GT_166110_20211107_20211117_02_T2	07/11/2021
30.	LC08_L1GT_166110_20220126_20220204_02_T2	26/01/2022
31.	LC08_L1GT_166110_20220227_20220309_02_T2	27/02/2022
32.	LC09_L1GT_165110_20221127_20221127_02_T2	27/11/2022
33.	LC09_L1GT_165110_20221213_20221213_02_T2	13/12/2022
34.	LC08_L1GT_165110_20230106_20230110_02_T2	06/01/2023
35.	LC09_L1GT_165110_20230215_20230215_02_T2	15/02/2023

To estimate surface melt and velocity over the NIS, Sentinel-1 Level-1 Interferometric Wide (IW) swath Ground Range Detected (GRD) and Single Look Complex (SLC) high-resolution data products were utilized (Nicolas et al., 2017). The data were acquired during the austral summer (November N, December D, January J, and February F) of the years 2019-2020, 2020-2021, 2021-2022, and 2022-2023 (Table 2). The IW swath mode, which covers a 250 km swath with a spatial resolution of 5 m x 20 m, is the primary acquisition mode over land. GRD data products are compressed and detected radar imagery that undergoes range compression elimination and is projected onto the ground range using the Earth ellipsoid model.

Table 2 Data used for estimating the surface melt extent and surface ice flow velocity over the Nivlisen ice shelf for the austral summer (November to February) of 2019-2020, 2020-2021, 2021-2022, and 2022-2023.

Sl.no	**Scene Id**	**Acquisition date**
Data used for estimating the surface melt extent over NIS		
1	S1A_IW_GRDH_1SSH_20191115T023418_20191115T023443_029915_0369CD_55DE	15/11/2019
2	S1A_IW_GRDH_1SSH_20191127T023418_20191127T023443_030090_036FE2_2BB3	27/11/2019
3	S1B_IW_GRDH_1SSH_20191203T023336_20191203T023401_019194_0243D0_B0CB	03-12-2019
4	S1B_IW_GRDH_1SSH_20191215T023335_20191215T023400_019369_024960_1015	15/12/2019

5	S1A_IW_GRDH_1SSH_20200102T023416_20200102T023441_030615_0381F3_3474	02/01/2020
6	S1A_IW_GRDH_1SSH_20200114T023416_20200114T023441_030790_038814_1839	14/01/2020
7	S1B_IW_GRDH_1SSH_20200201T023333_20200201T023358_020069_025FB7_EF7E	01/02/2020
8	S1A_IW_GRDH_1SSH_20200219T023415_20200219T023440_031315_039A65_08A1	19/02-2020
9	S1A_IW_GRDH_1SSH_20221111T023501_20221111T023526_045840_057BE6_EC4E	11/11/2022
10	S1A_IW_GRDH_1SSH_20221111T023436_20221111T023501_045840_057BE6_A389	11/11/2022
11	S1A_IW_GRDH_1SSH_20221124T195154_20221124T195219_046040_0582B5_8415	24/11/2022
12	S1A_IW_GRDH_1SSH_20221124T195125_20221124T195154_046040_0582B5_BA4E	24/11/2022
13	S1A_IW_GRDH_1SSH_20221206T195153_20221206T195218_046215_0588B1_BEA7	06/12/2022
14	S1A_IW_GRDH_1SSH_20221206T195124_20221206T195153_046215_0588B1_F402	06/12/2022
15	S1A_IW_GRDH_1SSH_20221218T195152_20221218T195217_046390_058EAD_B700	18/12/2022
16	S1A_IW_GRDH_1SSH_20221218T195123_20221218T195152_046390_058EAD_FA06	18/12/2022
17	S1A_IW_GRDH_1SSH_20230110T023458_20230110T023523_046715_059997_3386	10/01/2023
18	S1A_IW_GRDH_1SSH_20230110T023433_20230110T023458_046715_059997_3275	10/01/2023
19	S1A_IW_GRDH_1SSH_20230123T195151_20230123T195216_046915_05A065_31D5	23/01/2023
20	S1A_IW_GRDH_1SSH_20230123T195122_20230123T195151_046915_05A065_397E	23/01/2023
22	S1A_IW_GRDH_1SSH_20230204T195150_20230204T195215_047090_05A63A_1845	04/02/2023
23	S1A_IW_GRDH_1SSH_20230204T195121_20230204T195150_047090_05A63A_5CD8	04/02/2023
24	S1A_IW_GRDH_1SSH_20230227T023457_20230227T023522_047415_05B12C_3B84	27/02/2023
25	S1A_IW_GRDH_1SSH_20230227T023432_20230227T023457_047415_05B12C_CD6D	27/02/2023
Data used for estimating the Velocity of NIS		
26	S1A_IW_SLC__1SSH_20191103T023442_20191103T023509_029740_0363AB_D9AC	03/11/2019
27	S1B_IW_SLC__1SSH_20191109T023401_20191109T023428_018844_02389D_92F2	09/11/2019
28	S1A_IW_SLC__1SSH_20191115T023442_20191115T023509_029915_0369CD_8B41	15/11/2019
29	S1B_IW_SLC__1SSH_20191121T023401_20191121T023427_019019_023E3F_F7F0	21/11/2019
30	S1A_IW_SLC__1SSH_20191127T023442_20191127T023509_030090_036FE2_E574	27/11/2019

31	S1B_IW_SLC__1SSH_20191203T023400_20191203T023427_019194_0243D0_FAB4	03/12/2019
32	S1A_IW_SLC__1SSH_20191209T023442_20191209T023509_030265_0375E0_64EF	09/12/2019
33	S1B_IW_SLC__1SSH_20191215T023400_20191215T023427_019369_024960_CAD2	15/12/2019
34	S1A_IW_SLC__1SSH_20191221T023441_20191221T023508_030440_037BEE_5148	21/12/2019
35	S1B_IW_SLC__1SSH_20191227T023359_20191227T023426_019544_024EEF_367F	27/12/2019
36	S1A_IW_SLC__1SSH_20200102T023440_20200102T023507_030615_0381F3_A190	02/01/2020
37	S1B_IW_SLC__1SSH_20200108T023359_20200108T023425_019719_025480_FB94	08/01/2020
38	S1A_IW_SLC__1SSH_20200114T023440_20200114T023507_030790_038814_F294	14/01/2020
39	S1B_IW_SLC__1SSH_20200120T023358_20200120T023425_019894_025A13_68BB	20/01/2020
40	S1A_IW_SLC__1SSH_20200126T023440_20200126T023507_030965_038E3F_EDBD	26/01/2020
41	S1B_IW_SLC__1SSH_20200201T023358_20200201T023425_020069_025FB7_943E	01/02/2020
42	S1A_IW_SLC__1SSH_20200207T023439_20200207T023506_031140_039458_9678	07/02/2020
43	S1B_IW_SLC__1SSH_20200213T023357_20200213T023424_020244_026560_2907	13/02/2020
44	S1A_IW_SLC__1SSH_20200219T023439_20200219T023506_031315_039A65_B6F1	19/02/2020
45	S1B_IW_SLC__1SSH_20200225T023357_20200225T023424_020419_026AFD_7426	25/02/2020
46	S1B_IW_SLC__1SSH_20201103T023407_20201103T023434_024094_02DCD0_956F	03/11/2020
47	S1A_IW_SLC__1SSH_20201109T023449_20201109T023516_035165_041AE1_51C0	09/11/2020
48	S1B_IW_SLC__1SSH_20201115T023407_20201115T023434_024269_02E251_A870	15/11/2020
49	S1A_IW_SLC__1SSH_20201121T023448_20201121T023515_035340_0420FB_6D52	21/11/2020
50	S1B_IW_SLC__1SSH_20201127T023406_20201127T023433_024444_02E7CF_6AD3	27/11/2020
51	S1A_IW_SLC__1SSH_20201203T023448_20201203T023515_035515_0426FD_15B4	03/12/2020
52	S1B_IW_SLC__1SSH_20201209T023406_20201209T023433_024619_02ED6F_6DDF	09/12/2020
53	S1A_IW_SLC__1SSH_20201215T023448_20201215T023515_035690_042D08_D350	15/12/2020
54	S1B_IW_SLC__1SSH_20201221T023405_20201221T023432_024794_02F31D_0EA4	21/12/2020
55	S1A_IW_SLC__1SSH_20201227T023447_20201227T023514_035865_04331D_46AA	27/12/2020
56	S1B_IW_SLC__1SSH_20210102T023405_20210102T023432_024969_02F8C0_89FC	02/01/2021

57	S1B_IW_SLC__1SSH_20210114T023404_20210114T023431_025144_02FE5F_FBCA	14/01/2021
58	S1B_IW_SLC__1SSH_20210126T023404_20210126T023431_025319_0303F0_5DA1	26/01/2021
59	S1A_IW_SLC__1SSH_20210201T023445_20210201T023512_036390_044566_DCE5	01/02/2021
60	S1B_IW_SLC__1SSH_20210207T023403_20210207T023430_025494_030999_6127	07/02/2021
61	S1A_IW_SLC__1SSH_20210213T023445_20210213T023512_036565_044B7A_CF7A	13/02/2021
62	S1A_IW_SLC__1SSH_20210108T023446_20210108T023513_036040_043931_FE85	08/01/2021
63	S1B_IW_SLC__1SSH_20210219T023403_20210219T023430_025669_030F4F_D845	19/02/2021
64	S1A_IW_SLC__1SSH_20210225T023445_20210225T023512_036740_04518F_0730	25/02/2021
65	S1A_IW_SLC__1SSH_20211104T023454_20211104T023521_040415_04CA88_DE41	04/11/2021
66	S1B_IW_SLC__1SSH_20211110T023412_20211110T023439_029519_0385E3_26E7	10/11/2021
67	S1A_IW_SLC__1SSH_20211116T023454_20211116T023521_040590_04D0A4_A7FA	16/11/2021
68	S1B_IW_SLC__1SSH_20211122T023412_20211122T023439_029694_038B4A_B1F6	22/11/2021
69	S1A_IW_SLC__1SSH_20211128T023454_20211128T023521_040765_04D6A7_4D5C	28/11/2021
70	S1B_IW_SLC__1SSH_20211204T023412_20211204T023439_029869_0390C9_1DF3	04/12/2021
71	S1A_IW_SLC__1SSH_20211210T023453_20211210T023520_040940_04DCB7_0C1D	10/12/2021
72	S1A_IW_SLC__1SSH_20211222T023453_20211222T023520_041115_04E293_2528	22/12/2021
73	S1A_IW_SLC__1SSH_20220103T023452_20220103T023519_041290_04E873_97D8	03/01/2022
74	S1A_IW_SLC__1SSH_20220115T023452_20220115T023519_041465_04EE3B_0F03	15/01/2022
75	S1A_IW_SLC__1SSH_20220127T023451_20220127T023518_041640_04F420_2421	27/01/2022
76	S1A_IW_SLC__1SSH_20220208T023451_20220208T023518_041815_04FA34_BF7C	08/02/2022
77	S1A_IW_SLC__1SSH_20220220T023451_20220220T023518_041990_05004B_1D40	20/02/2022
78	S1A_IW_SLC__1SSH_20221111T023500_20221111T023527_045840_057BE6_C0BB	11/11/2022
79	S1A_IW_SLC__1SSH_20221123T023500_20221123T023527_046015_0581D3_0933	23/11/2022
80	S1A_IW_SLC__1SSH_20221205T023500_20221205T023527_046190_0587CA_3DE7	05/12/2022
81	S1A_IW_SLC__1SSH_20221217T023459_20221217T023526_046365_058DC1_4EF7	17/12/2022
82	S1A_IW_SLC__1SSH_20221229T023458_20221229T023525_046540_0593B0_ECE3	29/12/2022

83	S1A_IW_SLC__1SSH_20230110T023457_20230110T023524_046715_059997_13EE	10/01/2023
84	S1A_IW_SLC__1SSH_20230122T023457_20230122T023524_046890_059F7F_0374	22/01/2023
85	S1A_IW_SLC__1SSH_20230203T023457_20230203T023524_047065_05A554_7F94	03/02/2023
86	S1A_IW_SLC__1SSH_20230215T023456_20230215T023523_047240_05AB2F_5210	15/02/2023
87	S1A_IW_SLC__1SSH_20230227T023457_20230227T023523_047415_05B12C_7337	27/02/2023

4. Methodology

Figure 2 illustrates the complete process flow employed to acquire the seasonal patterns and fluctuations of surface melt, specifically in the form of melt ponds and SGLs over NIS. The utilization of an InSAR based displacement estimation technique is also incorporated within this process flow.

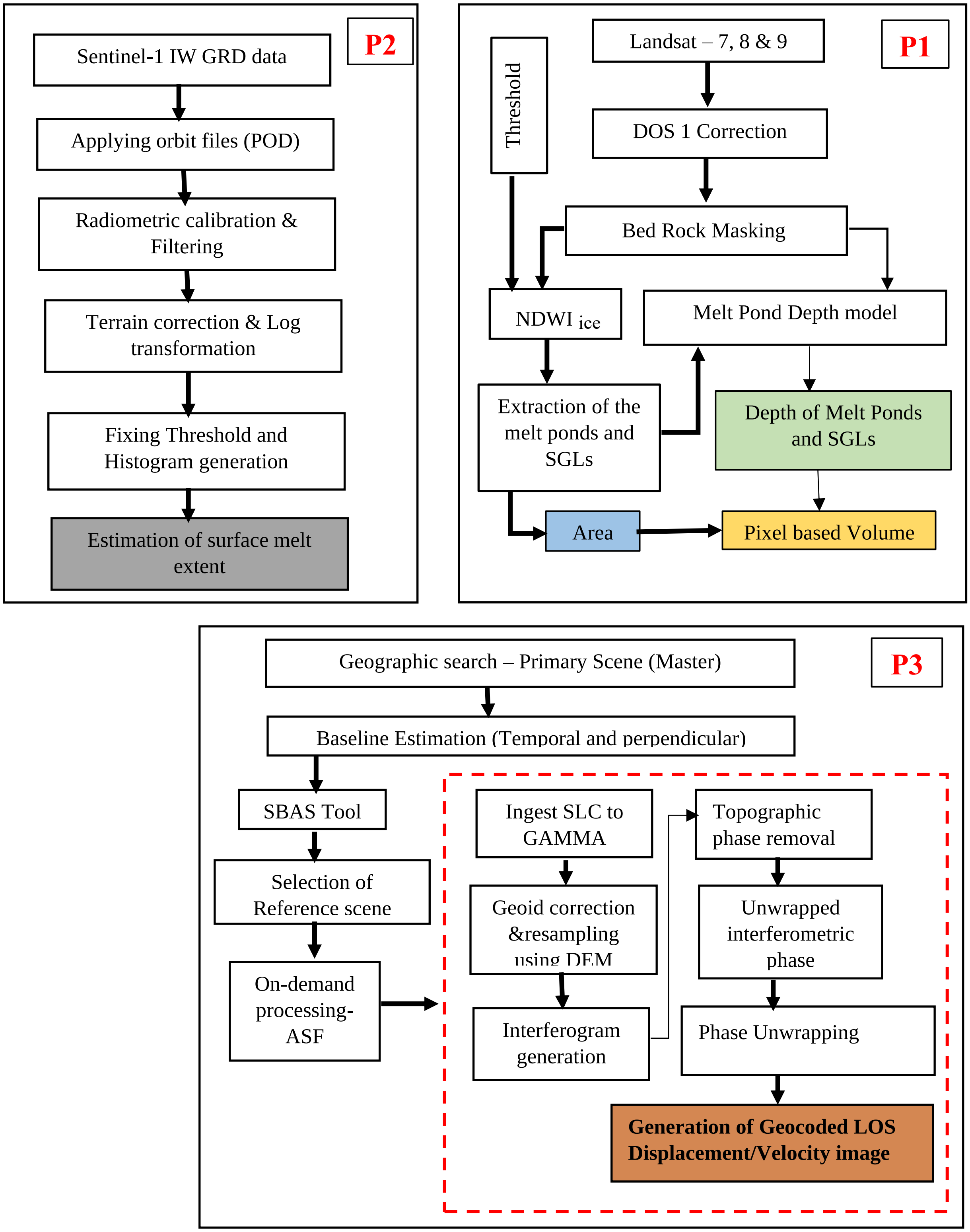

Fig. 2. Process flow – Estimation of surface melt extent (P1), depth of melt ponds and Supraglacial lakes using melt pond depth model, area and volume (P2), and ice flow velocity using (P3).

4.1. Melt Pond Depth Model

4.1.1. P1: Geometry of melt ponds/SGLs

The collected satellite data are available in Digital Number (DN), which must be converted to Top of Atmosphere (TOA) reflectance using Eq. 1 and Eq.2 for the visible (red and blue) bands.

$$\rho' = M_{Rf} Q_{Cal} + A_{Rf} \quad (1)$$

$$\rho = \frac{\rho'}{\cos(\theta_{SZ})} = \frac{\rho'}{\cos(\theta_{SE})} \quad (2)$$

Where Q_{Cal} is the visible band in DN format, ρ' is TOA reflectance without correction for the sun's angle, M_{Rf} is a multiply rescaling factor (band specific), A_{Rf} is an additive rescaling factor (band specific), ρ is TOA reflectance with correction for the sun's angle, θ_{SZ} is the sun's zenith angle, and θ_{SE} is the sun's elevation angle. The TOA blue and red bands were outfitted with bedrock masking.

4.1.2. Melt ponds and SGLs mapping

The modified Normalized Difference Water Index (NDWI_ICE) was computed using blue and red visible bands to map the melt ponds and SGLs present over the ice shelf (Eq. 3). The $NDWI_{ICE}$ is a modified normalized difference water index for icy locations that accentuates the spectral differential between unfrozen water and relatively arid snow/ice surfaces (Arthur, C.R. Stokes, et al. 2020). To obtain the melt ponds and SGLs cover over the ice shelf, $NDWI_{ICE}$ was used with a threshold of 0.25. The $NDWI_{ICE} > 0.25$ was used, and the threshold was adjusted by 0.01 based on the amount of water visible in the false colour composite (Arthur, C. Stokes, et al. 2020) (Dell et al. 2020). After thresholding, the areas of the melt ponds and SGLs were calculated using the vectorized raster.

$$NDWI_{ICE} = \frac{(BLUE_{Ref} - RED_{Ref})}{(BLUE_{Ref} + RED_{Ref})} \quad (3)$$

Where, $BLUE_{Ref}$ is the blue visible band reflectance and RED_{Ref} is the red visible band reflectance.

4.1.3. Lake depth estimation

To estimate the depth (L_d) of the melt ponds and SGLs, a multispectral data-based Melt Pond Depth (MPD) model (Eq. 4) was used (Philpot 1989) (Sneed and Hamilton 2007)(Pope et al. 2016) (Arthur et al. 2022)(Geetha Priya et al. 2022). The model employed in this study is grounded in the radiative transfer principle, which effectively simulates the interaction of light with various components, including the water column, the underlying aquatic bottom, and the surrounding environment. To calculate the depth of the water column, the model uses the rate of light attenuation in water, which is regulated by the absorption and scattering properties of the water. Furthermore, the method necessitates knowledge of the lake bottom's albedo, which is the reflectance of the lake bottom as a function of wavelength. The albedo is significant because it affects the amount of light reflected back to the surface, and hence the amount of light accessible for remote sensing sensors to detect. The proportion of dissolved and suspended materials affects the reflectance of optically deep water (L_d), which can impair the accuracy of the depth estimation.

$$L_d = \frac{[\ln(L_{br} - R_\infty) - \ln(R_{Ld} - R_\infty)]}{\alpha} \quad (4)$$

Where, L_{br} is peripherals reflectance of the lake, R_∞ is the reflectance of optically deep water, R_{Ld} is the reflectance of the water body, α is the attenuation constant

The L_{br} was calculated for each melt pond/SGL in every scene by averaging two pixels buffer. The mean variation between using $R_\infty = 0$ (i.e., reflectance from open ocean water) and using R_∞ values obtained from the lakes in the scenarios is less than 10%. As a result, the R_∞ value was considered to be nil for all scenes. The Red reflectance undergoes a more pronounced attenuation in water when compared to blue reflectance. This phenomenon manifests as more substantial and measurable alterations in the Red reflectance over water, surpassing the changes observed for other wavelengths. Because of the spectral characteristic of water bodies, red band reflectance was explored for R_{Ld}. The Landsat-8 and Landsat-9 have OLI1 and OLI2 sensors respectively, due to the same characteristics of both the sensors (Masek et al. 2020), the same attenuation constant of 0.7507 was used for the model. As for the Landsat-7 data which has an ETM+, an attenuation constant of 0.8049 was used for the Red band.

The melt pond depth model used to extract the depth of the lakes considers the lake bottom albedo to be homogeneous, and there is no scattering due to undissolved matter (Yuan et al. 2020). In this work only non-ice-covered lakes were considered for depth estimation.

4.2. P2: Estimation of Surface melt extent

To assess the extent of surface melt on NIS, the Sentinel-1 SAR data was processed using a developed Science Toolbox Exploitation Platform (SNAP) algorithm (Fig. 2., P1). The processing involved stacking multiple SAR images and adjusting the GRD outputs with a temporal baseline, utilizing an accurate orbit file (Rakshita et al. 2023). In order to obtain the radar backscatter bands, the images were radiometric calibrated across the entire region. This calibration process converted the digital SAR image pixel values into backscatter (σ^0) (Zhu et al. 2023). Following calibration, a Lee filter with a window size of 5 x 5 pixel was applied to remove speckle noise, which arises from interference between scattered light beams when illuminated by laser light. Geometric distortions and topographic variations were then rectified using Range-Doppler Terrain Correction with a GETASSE30 DEM (Safa and Flouzat 1989). Subsequently, the geometrically adjusted σ^0 image was logarithmically transformed to decibels. To determine the extent of surface melt, the histogram generated from σ^0values projected in decibels was thresholded (Lund et al. 2022), following the method outlined in Jewell Lund et al., 2022. The resulting binary image was used to digitally delineate the area of interest using the mask manager. It is important to note that this threshold value varied from one image to another based on the specific histogram characteristics.

4.3. P3: Surface ice velocity

The Alaska satellite Facility's mission provides access to On Demand services (https://hyp3-docs.asf.alaska.edu/using/vertex/) that build SAR interferometry products from Sentinel-1 data to make SAR data more available to the research community. Sentinel-1 SLC pairs were submitted for processing through ASF's data search, and the results of the On Demand process was download. Through a geographic search in Alaska Vertex, the reference scene and a secondary scene were selected to build an interferogram.

The Baseline tool aids in the identification of data that fall within a reasonable range of perpendicular baseline values, allowing them to be coupled with the reference scene for InSAR processing. In order for the phase measurements to be coherent enough for interferometry, the scenes must be obtained with high temporal resolution. SBAS employs a large number of interferograms derived from SAR images recorded over a long period of time, with each individual InSAR pair having a relatively small-time delay between acquisitions. A variety of short baselines were used, which allows each reference scene to be coupled with several secondary scenes. The On-Demand InSAR method includes pre-and post-processing of data sets. The SLC data sets were primarily imported into GAMMA format. Geoid correction was performed using the research area's DEM dataset. After resampling, the overlapping bursts for the input scenes were estimated. The swath and bursts were mosaicked, and an initial look-up table was created to represent an unwrapped image for SLC co-registration. Thereafter, the interferogram was created, matched, refined, and iterative co-registration with a look-up table was performed. To compute a co-registration offset based on the burst overlap, the Earth curvature, and topographic phase were subtracted. To estimate LOS displacement, phase unwrapping was carried out using Statistical-cost, Network-flow Algorithm for Phase Unwrapping (SNAPHU). Post-processing entails creating geocoded Geotiff outputs of velocity (Sivalingam et al. 2022).

5. Results and Discussion

5.1 Dynamics of melt ponds and SGLs

The depth of the melt ponds and SGLs over the ice shelf was estimated using the process flow discussed in section 4.1 (Fig 2., P2). To ensure accurate volume estimation and mitigate potential overestimation or underestimation, a pixel-based approach was employed for each melt pond and SGL (Land et al. 2023)(Leppäranta et al. 2020). This approach utilized the depth profile derived from the MPD model. By considering the individual pixel values within the water body, a more precise estimation of volume was achieved, enhancing the reliability of the results. This approach helped to overcome the limitations associated with conventional estimation methods and provided a more accurate representation of the actual volume of each melt pond and SGL. The study has been carried out for austral summers of 2000–2023 during the period of peak melt. The model-based depth is shown in Fig. 3-11. Fig. 3 represents the depth estimates for the period 2000–2014.

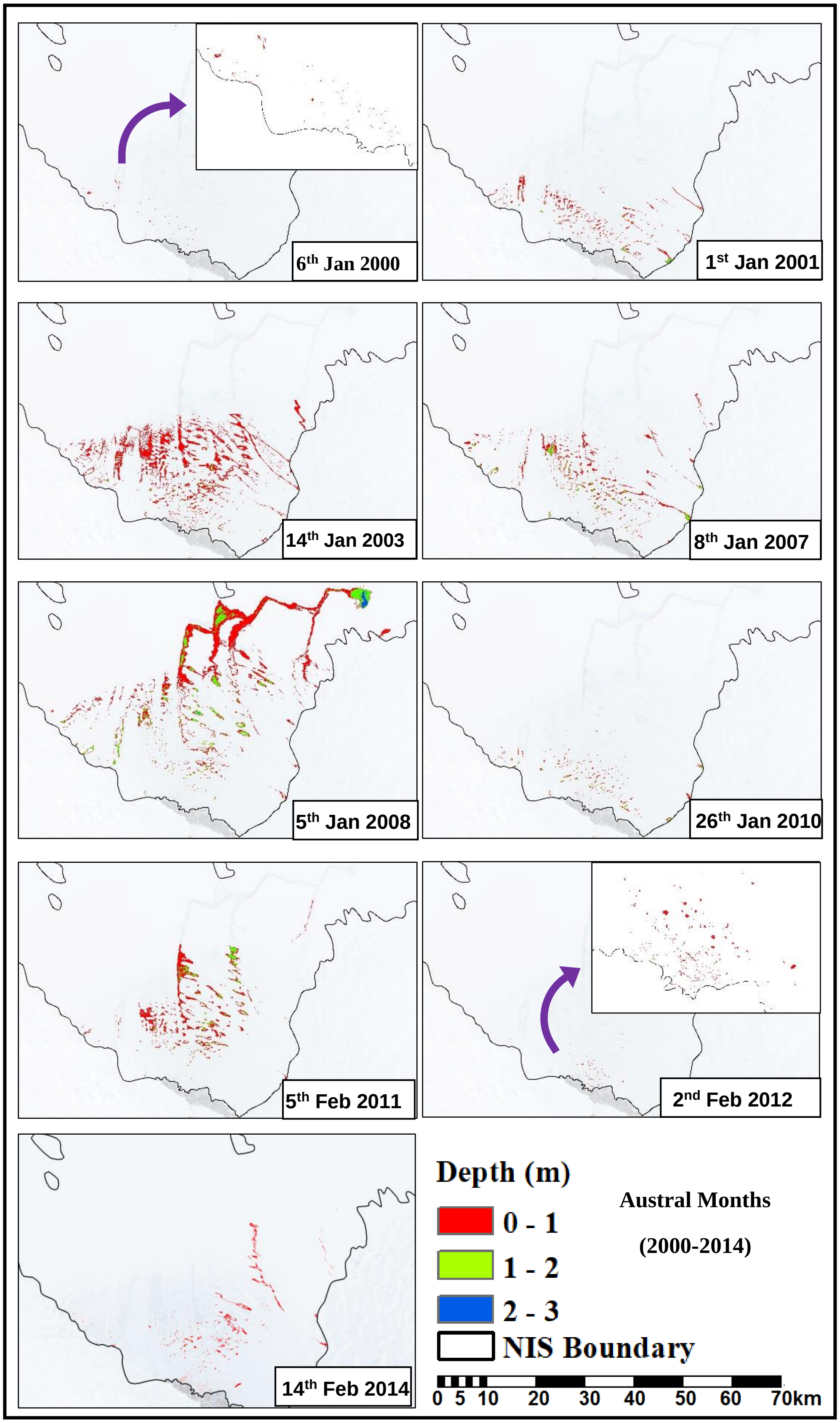

Fig. 3. Model-based melt pond depth at peak melting in the austral summers of 2000-2014.

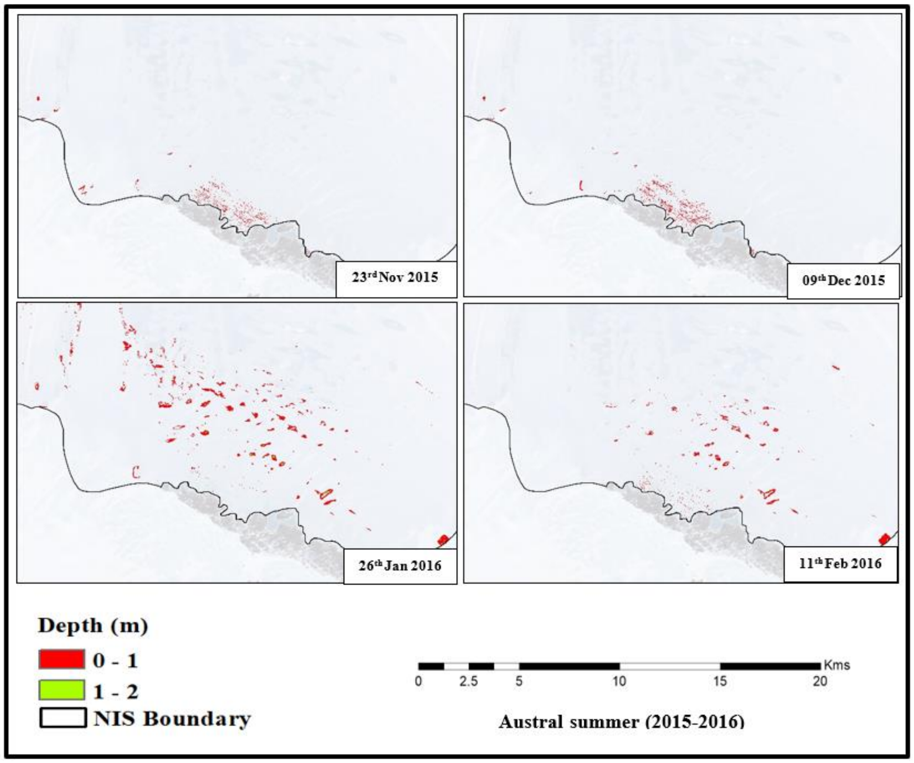

Fig. 4. Model-based melt pond depth model for the austral summer of 2015–2016.

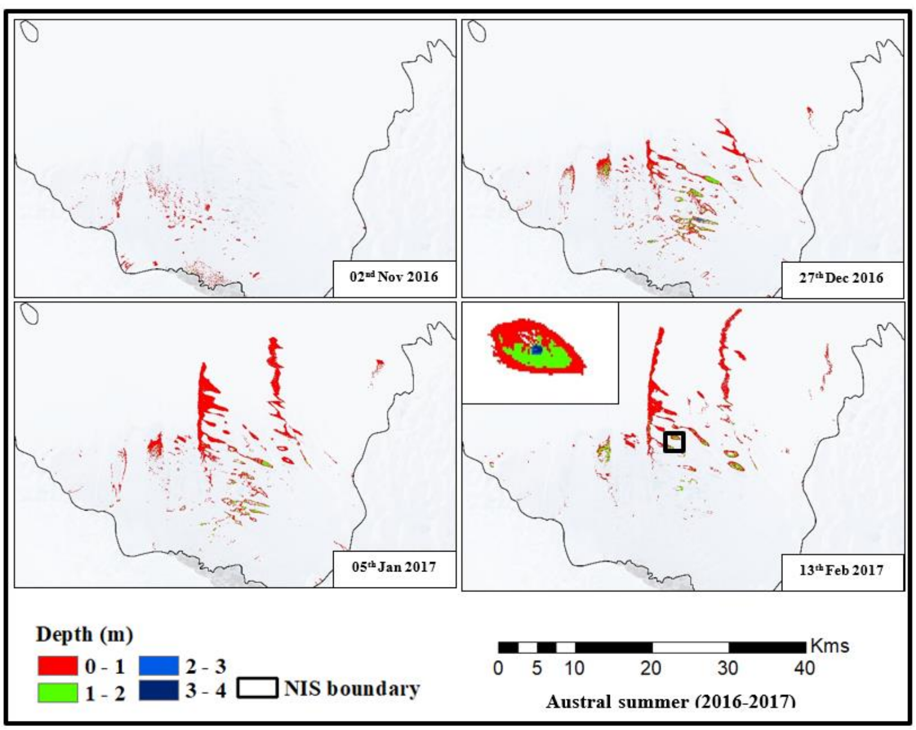

Fig. 5. Model-based melt pond depth for the austral summer of 2016–2017.

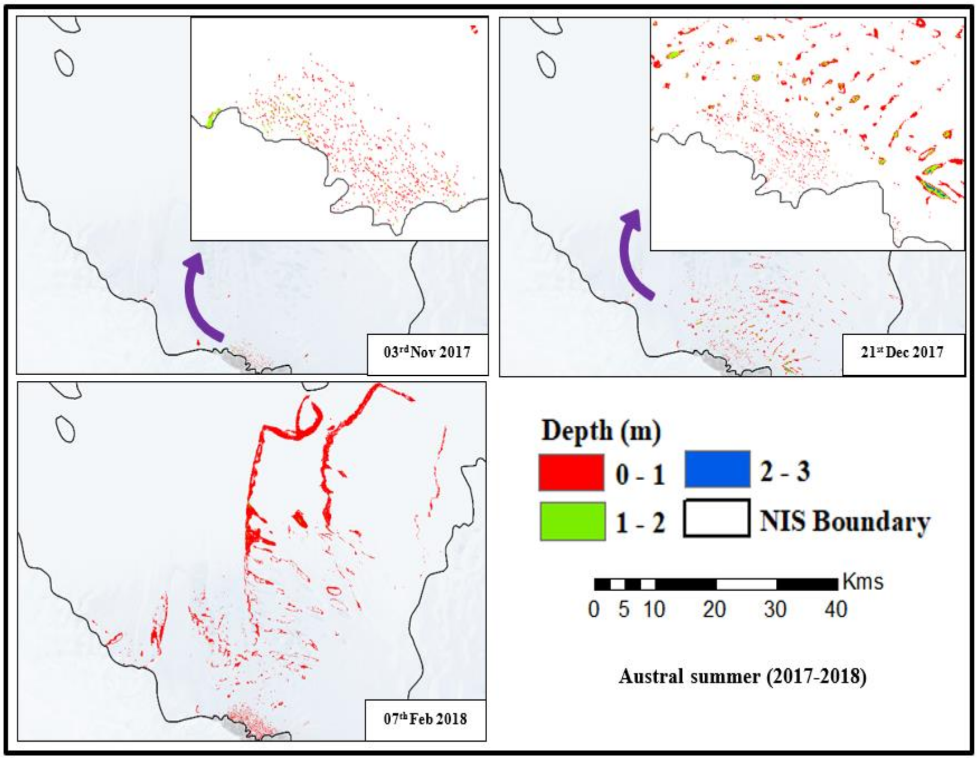

Fig. 6. Model-based melt pond depth model for the austral summer of 2017–2018.

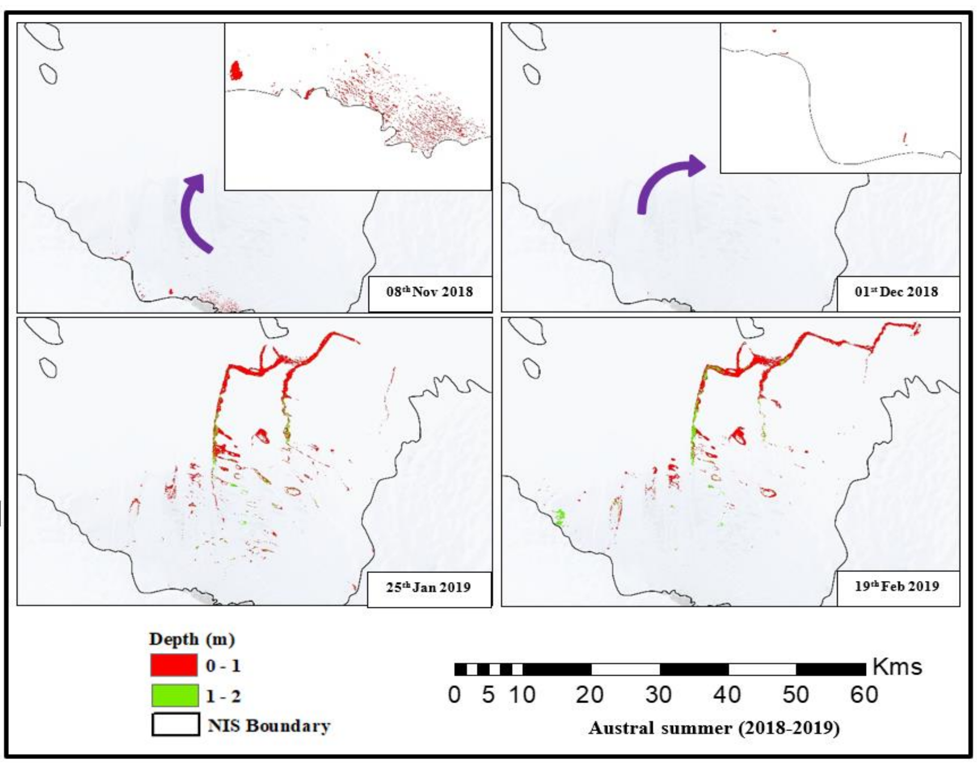

Fig. 7. Model-based melt pond depth model for the austral summer of 2018–2019.

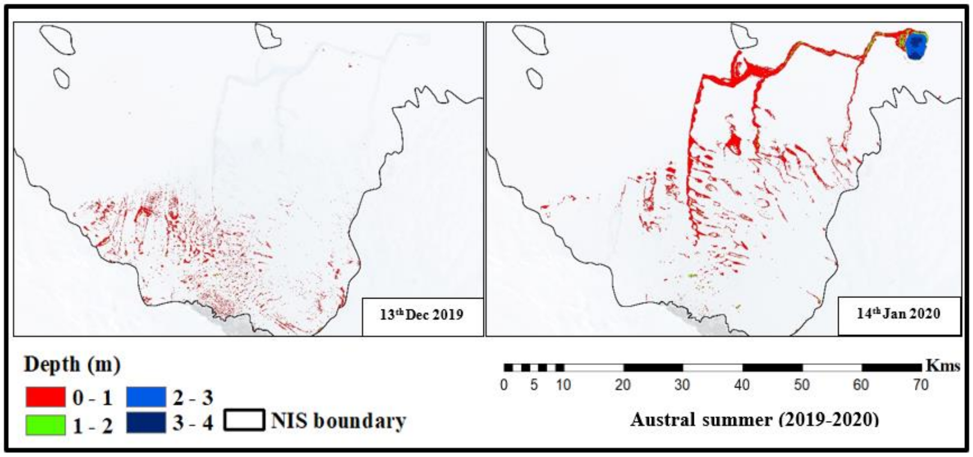

Fig. 8. Model-based melt pond depth for the austral summer of 2019–2020.

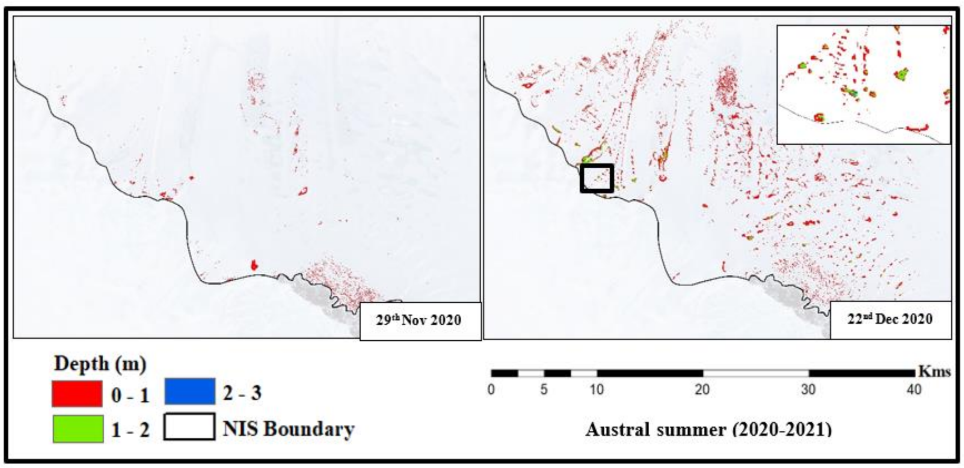

Fig. 9. Model-based melt pond depth for the austral summer of 2020–2021.

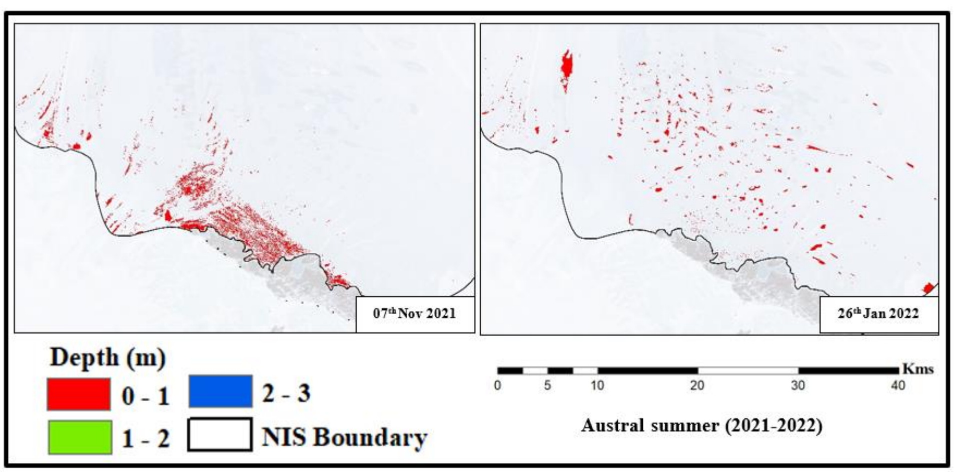

Fig. 10. Model-based melt pond depth for the austral summer of 2021–2022.

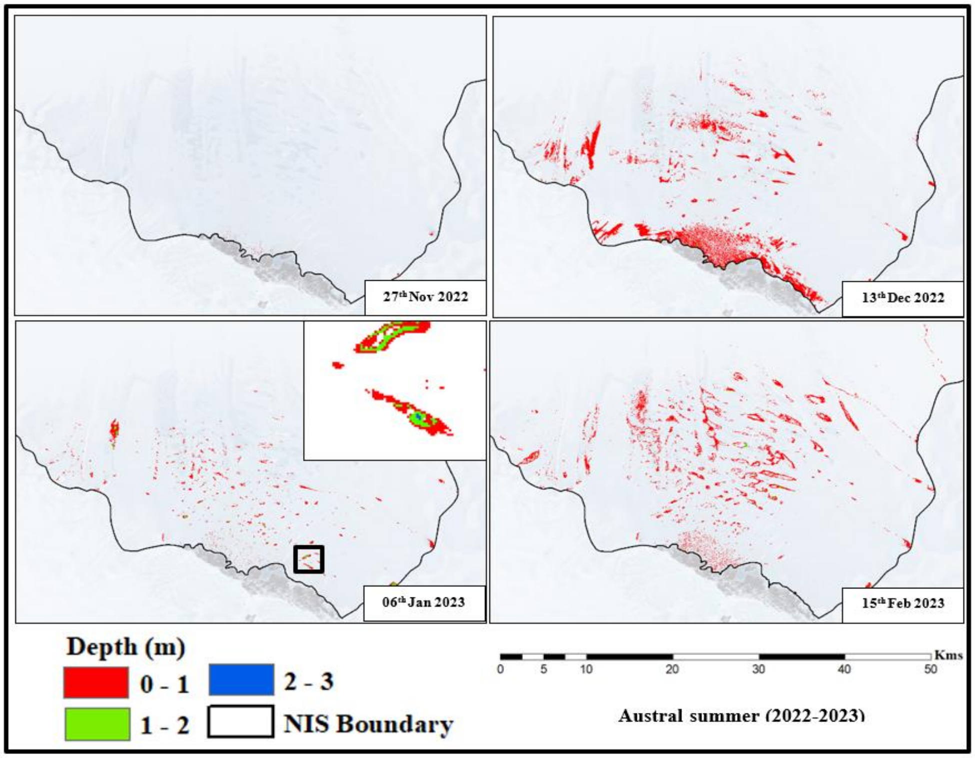

Fig. 11. Model-based melt pond depth for the austral summer of 2022–2023.

The analysis of melt ponds and SGLs area revealed that the total area remained relatively low (<1 sq. km), during November and December over the period 2000-2014. However, a significant increase in meltwater volume was observed during the period from early to late January and February, representing the peak meltwater volume of the season (Hall et al. 2009)(Orr et al. 2022)(Vaňková et al. 2021). A consistent melting pattern with increased formation of melt ponds and SGLs were observed for NDJF over the period 2015-2023 (Fig 3-11). This trend is illustrated in Table 3 and Figures 12-13, which demonstrates the temporal variations in meltwater volumes over the study period. The findings highlight the seasonal variability in meltwater accumulation and provide valuable insights into the timing and magnitude of peak meltwater volume in the study area.

Table 3 Depth, area, and volume of SGLs on Nivlisen ice shelf for the austral summer (November to February) of 2000-2023

Date	Depth (m)		Area (km^2)	Volume (m^3)
	Maximum	Average		
06/01/2000	2.30	0.002	1.203	2070.52
01/01/2001	2.25	0.006	27.081	2033.63
14/01/2003	1.68	0.010	140.82	1516.46
18/01/2007	2.23	0.005	36.18	2007.38
05/01/2008	2.83	0.025	187.18	2547.56
26/01/2010	2.29	0.002	10.26	2050.51
05/02/2011	2.11	0.010	55.83	1902.38
02/02/2012	1.28	0.005	1.05	1148.79
14/02/2014	1.83	0.003	38.73	1643.41
23/11/2015	1.31	0.005	1.66	1179.34
09/12/2015	1.09	0.001	2.13	979.89
26/01/2016	2.54	0.004	17.19	2278.52
11/02/2016	1.48	0.003	24.99	1329.03
02/11/2016	2.53	0.001	12.92	2280.56
27/12/2016	4.15	0.004	44.86	3736.76
05/01/2017	2.48	0.005	64.86	2235.89
13/02/2017	3.53	0.004	47.54	3175.78
03/11/2017	2.80	0.391	131.49	2520.00
21/12/2017	3.06	0.678	12.19	2750.92
07/02/2018	2.94	0.480	110.68	2250.67
08/11/2018	1.69	0.001	2.96	1520.00
01/12/2018	1.12	0.003	0.11	1005.00
25/01/2019	3.70	0.015	54.77	3329.00
19/02/2019	3.28	0.008	55.55	2952.00
13/12/2019	2.56	0.003	55.15	2308.87
14/01/2020	3.57	0.015	132.64	3213.62
29/11/2020	1.87	0.003	4.35	1684.35
22/12/2020	2.49	0.002	21.70	2245.90
7/11/2021	1.90	0.004	21.32	1708.10
26/01/2022	1.07	0.188	118.47	964.90
27/11/2022	1.27	0.008	22.01	1137.45
13/12/2022	1.67	0.005	38.81	1505.51
06/01/2023	2.68	0.002	170.69	2417.24
15/02/2023	2.09	0.004	89.53	1880.02

The distribution of melt ponds and SGLs over NIS tends to be clustered, with a greater concentration of ponds were observed on the southern grounding zone. Conversely, melt ponds and SGLs are nearly absent in the vicinity of the central part of the ice shelf, where surface melt rates are at their lowest. The results were analyzed in relation to the weather data obtained for the study area (weather station No. 89512), from the Meteostat database which provides comprehensive weather information for various weather stations and locations worldwide (https://meteostat.net/en/station/89606?t=2022-11-01/2023-02-28). Figure 14 shows the temperature trend for the study region, as obtained from Meteostat for the years 2000-2023.

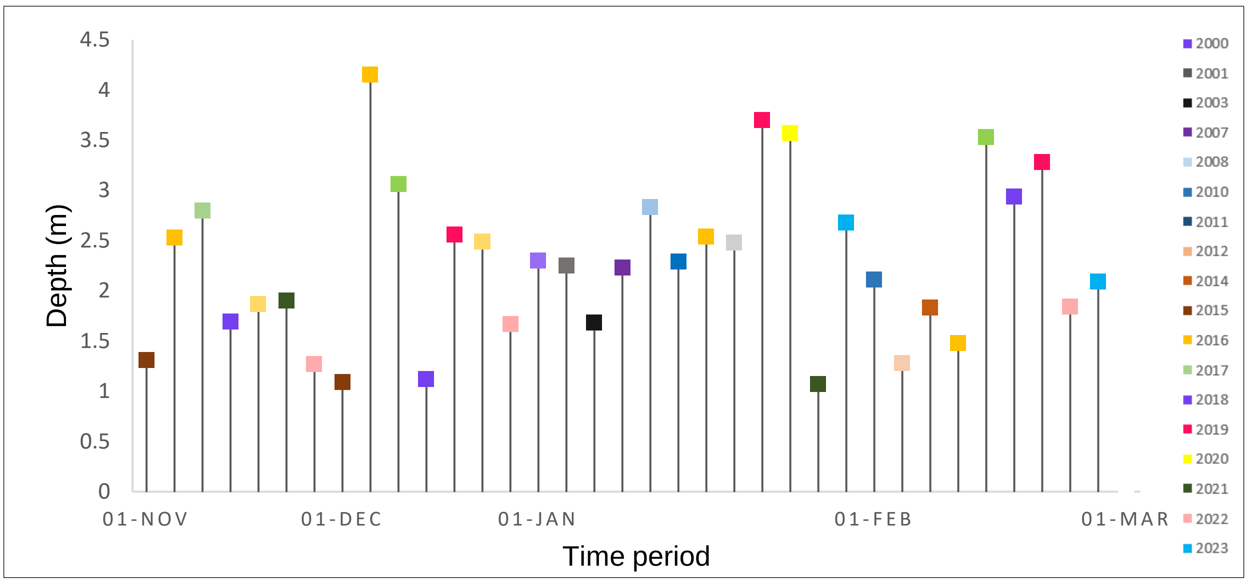

Fig. 12. Maximum depth during austral summers of 2000-2023.

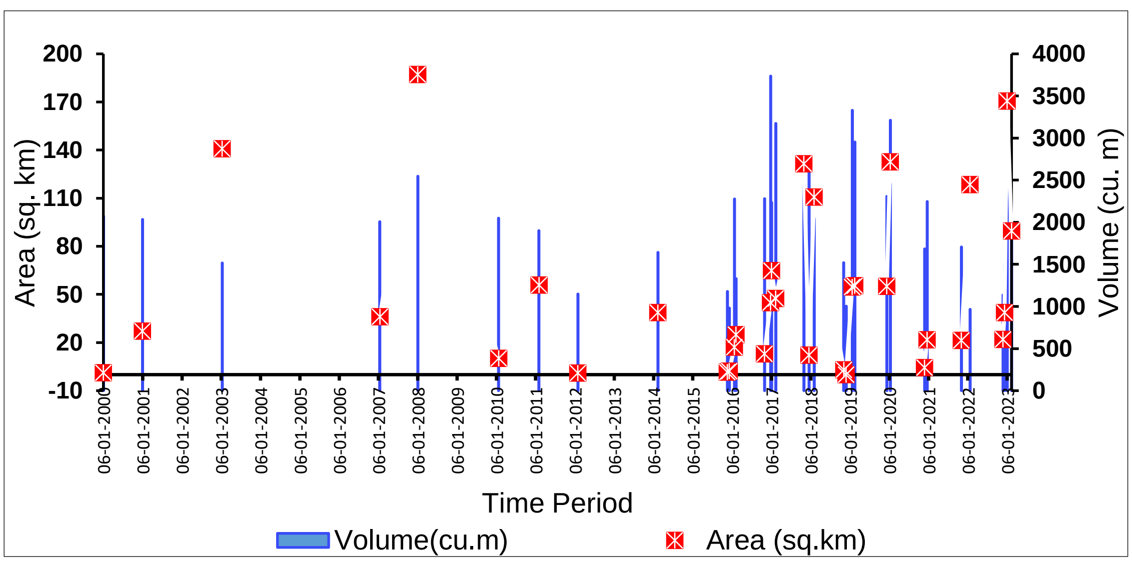

Fig. 13. Area and volume during austral summers of 2000-2023

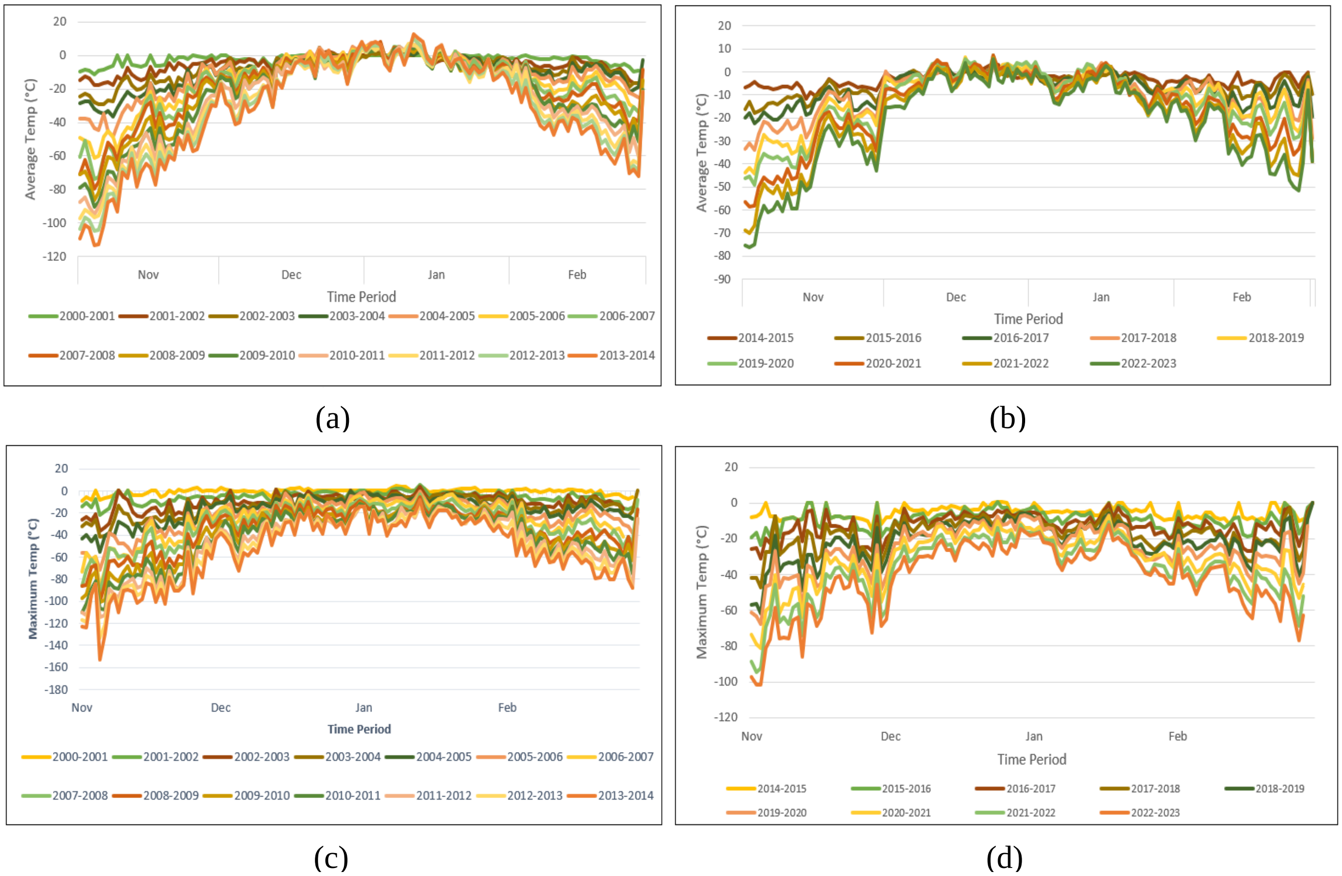

Fig. 14. (a) The average temperature for the austral summers of 2000 to 2014 (b) The average temperature for the austral summers of 2014 to 2023 (c) The maximum temperature for the austral summers of 2000 to 2014 (d) The maximum temperature for the austral summers of 2014 to 2023**.**

On January 6, 2000, the melt ponds and SGLs reached a maximum depth of 2.3 m and a volume of 2,070.52 m^3. The total area covered was 1.203 km^2. Similarly, on January 1, 2001, the maximum depth of the melt ponds and SGLs was 2.25 meters, with an area of 27.081 km^2 and a volume of 2,033.63 m^3. Despite an average temperature of -1.1°C on January 14, 2003, the maximum depth of melt ponds and SGLs was estimated to be 1.68 m. The area covered was 140.83 km^2, with a volume of 1,516.46 m^3. The research highlights a steady decrease in the maximum depth and volume of melt ponds and SGLs in 2003, while the area of the melt pond increased compared to 2000 and 2001. On January 18, 2007, the highest depth and volume of melt ponds and SGLs were 2.23 m and 2,007.38 m^3, respectively. The total area covered was 36.18 km^2. The maximum depth and volume increased compared to the previous year (2003), possibly due to an increase in the average and maximum temperatures by 0.3°C and 3.6°C, respectively. On January 26, 2010, the maximum depth and volume of the melt ponds and SGLs were 2.29 m and 2,050.51

m^3, respectively, covering a total area of 10.26 km^2. Between 2000 and 2010, the highest values for depth, area, and volume were recorded on January 5, 2008, measuring approximately 2.83 m, 187.18 km^2, and 2,547.56 m^3, respectively. On February 5, 2011, the maximum depth and volume of melt ponds and SGLs decreased, while the area increased to 55.83 km^2, which was 5.4 times larger than the lake area in January 2010. Similarly, on February 2, 2012, the depth, area, and volume of SGLs considerably decreased to 1.28 m, 1.05 km^2, and 1,148.79 m^3, respectively, with a maximum temperature of 10°C. This reduction may have been caused by high katabatic winds and the wind chill factor. On February 14, 2014, with a decline in maximum and average temperatures compared to the previous year (2012), the maximum depth and volume of melt ponds and SGLs were 1.83 m and 1,643.41 m^3, respectively, covering a total area of 38.73 km^2.

During the austral summers from 2015 to 2016, there were slight variations in the maximum depth, area, and volume of melt ponds and SGLs. The highest recorded maximum depth and volume were 2.54 m and 2,278.52 m^3, respectively, on January 26, 2016. The maximum area of 24.99 km^2 was recorded on February 2, 2016. These variations could be attributed to changes in both the maximum (ranging from 1.9°C to -0.8°C) and average temperatures (ranging from −0.6°C to −3.8°C). For the austral summers of 2016 to 2017, the highest depth (4.15 m) and volume (3,736.76 m^3) of melt ponds and SGLs were observed on December 27, 2016. This increase was due to the highest recorded average and maximum temperatures of 3.2°C and 5.5°C, respectively. In the austral summers of 2017 to 2018, the estimated maximum depth and volume of SGLs were 3.06 m and 2,750.92 m^3, respectively. The lake area was reduced to 12.19 km^2. These higher values were associated with the highest average and maximum temperatures recorded on December 21, 2017, reaching 1.3°C and 4.2°C, respectively. For the austral summers of 2018 to 2019, the estimated maximum depth and volume of SGLs were 3.7 m and 3,329 m^3, respectively. The lake area expanded to 54.77 km^2, with an average temperature of −2.4°C on January 25, 2019. Despite the relatively low average temperature, the predicted volume was significant due to temperature fluctuations during the peak melt season. During the austral summers of 2019 to 2020, the highest maximum depth (3.57 m) and volume (3,213.62 m^3) of melt ponds and SGLs were observed on January 14, 2020, compared to December 13, 2019. This increase was attributed to the highest recorded average and maximum temperatures of 1.3°C and 2.7°C, respectively, on January 14, 2020.

During the austral summers from 2020 to 2021, the maximum depth, area, and volume of SGLs increased by a factor of 1.33, 4.98, and 1.33, respectively, on December 22, 2020. This increase was attributed to higher average and maximum temperature records of 0.3°C and 3°C, respectively. For the austral summers of 2021 to 2022, larger values of SGLs were recorded with a depth of 1.9 m and a volume of 1,708.1 m^3 on November 7, 2021. However, the volume decreased to 964.9 m^3 on January 26, 2022, which was roughly 1.7 times the lake area on November 7, 2021. Despite a temperature increase from −2.6°C (on November 7, 2021) to 2.1°C (on January 26, 2022), the volume of the lake decreased. This reduction could be attributed to water draining through internal fissures and drainage canals. During the austral summers of 2022 to 2023, higher values of SGLs depth, area, and volume were observed on January 6, 2023, reaching 2.68 m, 170.69 km^2, and 2,417.24 m^3, respectively. However, by February 15, 2023, these values decreased to 2.09 m, 89.53 km^2, and 1,880.02 m^3, respectively, due to a drop in temperature from 2.2°C in January to −2.5°C in February. The drainage mechanism contributed to the reduction in the volume of the SGLs after January 2023.

According to Arthur et al. (2020), the surface area of melt ponds and SGLs on the ice shelf generally expands during the austral summer months of December and January, reaching a maximum value in late December to early January. As the melt season progresses, there is a gradual contraction in the total lake area, which reaches its minimum towards the end of February. The depth of the lakes follows a similar seasonal trend, with the deepest lakes typically observed during the late December to early January period. This pattern is consistent with the changes in the total lake area, as both the depth and surface area of the lakes are influenced by the melting and freezing dynamics of the ice shelf. Towards the end of February, the melt ponds and SGLs start to refreeze, resulting in a reduction in lake area and volume. These melt ponds and SGLs on ice shelves have significant implications for global sea levels, ocean circulation patterns, and marine ecosystems (Arthur, C. Stokes, et al. 2020). With ongoing global warming, it is anticipated that the formation of melt ponds and SGLs will increase, amplifying their impacts on Earth's systems. Therefore, it is crucial to monitor and comprehend the consequences of these melt ponds and SGLs (Mahagaonkar, A et al. 2023).

During the austral summer months, surface lakes are commonly found in the inland areas of the ice shelf, while the central part of the ice shelf typically experiences minimal formation of SGLs. These cyclic variations in the total lake area lead to fluctuations in meltwater volume throughout the melt season. The increased surface runoff resulting from higher melt rates establishes a linear relationship between SGL area and volume, contributing to significant fluctuations during the austral summer. When compared to the year 2000, there has been an increase in SGL depth and area, accompanied by a subsequent rise in volume. Among the studied years, 2016, 2017, 2019, and 2020 exhibit maximum SGL depth. The years 2008, 2016, and 2020 show maximum volume with a gradual increase in area. The highest area is observed in January 2008 and 2023 during the studied austral summers. The area experiences a significant increase from January 2022 to January 2023, followed by a reduction from in mid-February 2023. These findings align with the expectations of the research community, as reported by the Intergovernmental Panel on Climate Change (IPCC) in 2019 and Bell et al. (2018). They predict that the coverage area and volume of surface meltwater on Antarctic ice shelves will increase in response to rising atmospheric temperatures.

5.2. Seasonal surface melt and surface ice flow velocity variations of the NIS: Limitations and Focus on austral summers 2019-2023

This study aims to estimate the seasonal surface melt and surface ice flow velocity of the NIS in East Antarctica, specifically focusing on the austral summer period spanning from November to February. The study is constrained to analyzing the seasonal surface melt patterns and variations in surface ice flow velocity exclusively during the austral summers of 2019-2023. This is due to the following:

- The MEaSUREs Program of NASA (https://nsidc.org/aiv) provides high-resolution, digital mosaics of ice motion in Antarctica. These mosaics are created using data from multiple satellite interferometric and synthetic-aperture radar systems. The available data covers the period from 1996 to 2016, allowing for an annual analysis of ice motion in Antarctica at a detailed scale.
- The availability of Sentinel-1 data begins from 2014 onwards, and processing the line of sight (LOS) displacement/velocity of the ice surface requires a suitable InSAR pair. However, no suitable pairs were found for the austral summer period from 2014 to 2019 over the study region. Suitability is determined based on the smallest possible perpendicular and temporal baseline with a similar polarization between the master and slave images.
- For the period of austral summers from 2000 to 2014, suitable InSAR pairs from ERS (European Remote Sensing satellite), ALOS PALSAR (Advanced Land Observing Satellite

Phased Array L-band Synthetic Aperture Radar), and RADARSAT (Radar Satellite) satellites were also unavailable/limited over the study area.

5.3. Seasonal surface melt extent

Surface melt-water production is believed to increase as winds warm adiabatically while descending to the grounding zone, lowering humidity and raising near-surface air temperatures. On East Antarctic ice shelves, surface melt has been linked to severe katabatic-wind-induced scouring of blue-ice areas (Bell et al. 2017). Utilizing remote sensing techniques and datasets for monitoring surface melt provides valuable insights into ice shelf stability (Tuckett et al. 2019) (Konovalov 2021). The surface melt extent (SME) map will prove beneficial for future climate change research and analysis (Alley 2017). Using the process flow discussed in section 4.2, the surface melt extent was estimated for the austral summers of 2019-2020, 2020-2021, 2021-2022, and 2022-2023 and shown in Figure 15. Figure 16 shows the surface melt extent map generated for 2022-2023 for representation purposes. For all the austral summers of 2019-2023, the surface melt has been detected in the northwest (ice front) and southern (grounding line) parts of the shelf above the Schirmacher Oasis, whereas the center of the shelf has remained dry for most of the melt seasons. The study region's precipitation trend, obtained from Meteostat, is depicted in Figure 17, while the temperature pattern is illustrated in Figure 14. These figures serve as essential tools for interpreting the extent of surface melt. By analyzing the precipitation data and temperature patterns, we gain valuable insights into the factors influencing surface melting in the study region.

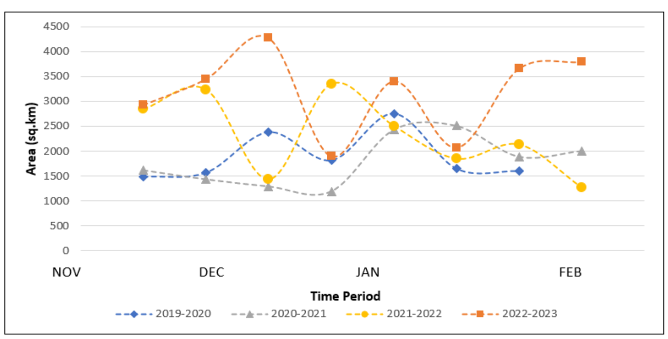

Fig.15. The surface melt extent (SME) over NIS, for the austral summers 2019-2020, 2020-2021, 2021-2022, 2022-2023.

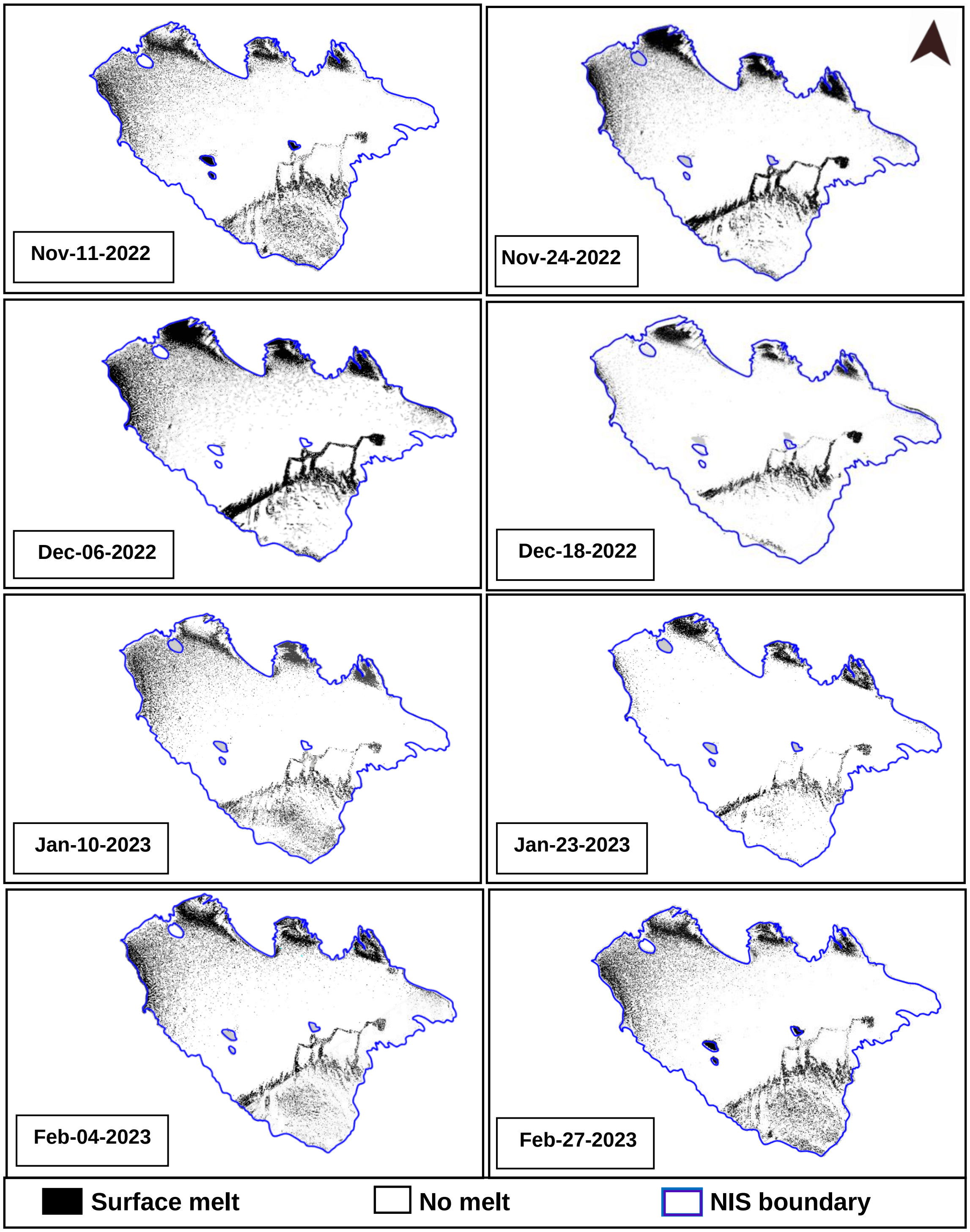

Fig. 16. The surface melt extent (SME) map over NIS for the austral summer 2022-2023.

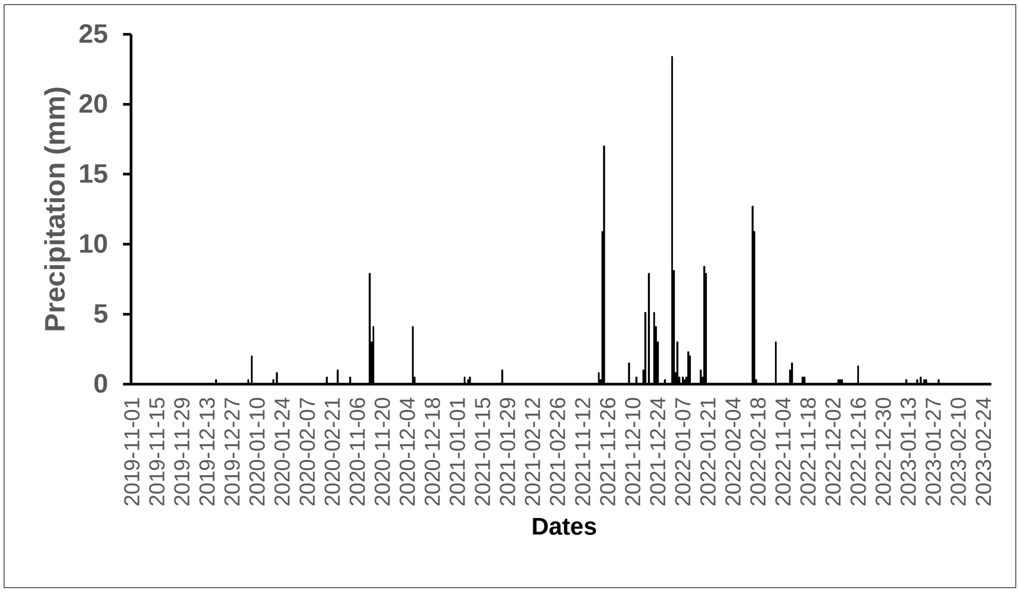

Fig.17. Precipitation (mm) for the four austral summers considered for SME (2019-2020, 2020-2021, 2021-2022, and 2022-2023)

5.3.1. Surface melt during the austral summer 2019-2020

In November 2019, there was a notable surge in surface melting, characterized by an average surface melt area of 1,531 km^2. The mean temperature fluctuated between –7.9°C and –1.2°C during this period. Transitioning to December 2019, the mean temperature ranged from –3.9°C to 2.9°C, coinciding with a significant increase in the average surface melt area, which expanded to 2,102 km^2. On December 15, 2019, the highest recorded mean temperature of 1.6°C was observed. Moving into January 2020, which marked the peak of the melt season, the average extent of surface melt reached 2,202 km^2, exhibiting a slight rise compared to December 2019. The monthly average temperature ranged from –5°C to 2.7°C, leading to a comparatively lower degree of melting that fell within a similar range as December 2019. However, February 2020 witnessed a substantial escalation in the average surface melt area, totalling 3,086 km^2, surpassing the levels observed in January 2020. This pronounced increase in melting coincided with an average temperature range of –6.8°C to 0.6°C. The highest surface melt during February 2020 can potentially be attributed to the albedo effect, which induces a positive feedback mechanism that enhances melting processes (Arthur, C. Stokes, et al. 2020)(Trusel et al. 2012).

5.3.2. Surface melt during the austral summer 2020-2021

In November 2020, the estimated surface melt area was approximately 1,519 km^2. The mean temperature during that period ranged from –13.1°C to –0.3°C, while recorded precipitation amounted to 4.1mm. These measurements closely align with the surface melt area estimates from November 2019. During December 2020, a significant change in melting dynamics was observed, primarily driven by temperature fluctuations. The estimated average surface melt area was around 1,239 km^2, indicating a decrease compared to the previous month. This decrease in surface melt area coincided with a rise in mean temperature from –4.8°C to 1.4°C. However, it is worth noting that despite the increase in average temperature, the reduction in surface melt area could be attributed to the influence of high freezing winds and variations in the wind chill factor (source: www.yr.no), which ranged from –7°C to –8°C during this period. In January 2021, the average extent of surface melt expanded to 2,474 km^2, signifying the peak melt season. This increase in surface melt area was accompanied by a rise in the average temperature from –6.1°C to 3.8°C. In February 2021, the average surface melt area amounted to 1,947 km^2, representing a decrease compared to February 2020. The mean temperature ranged from –8.4°C to –1.4°C during this month. These findings indicate that the surface melting observed in February 2021 accounted for only two-thirds of the extent observed during February 2020.

5.3.3. Surface melt during the austral summer 2021-2022

During the month of November 2021, the surface melting had increased with an average surface melt of 1,618 km^2 with a mean temperature range from –12.3°C to –1.5°C. This represents an approximately 100 km^2 increase compared to the surface melt observed in November 2019 and 2020. December 2021 experienced a significant rise in the melt area, predominantly attributed to the upsurge in temperature. The average surface melt area expanded to approximately 2,392 km^2, while the mean temperature exhibited a range of –4.5°C to 0.9°C. In January 2022, despite being the peak melt season, the average extent of surface melt amounted to 2,177 km^2. The mean temperature fluctuated from –4.6°C to 0.9°C. The diminished surface area undergoing melting during this period may be attributed to the recorded precipitation of 4.1mm in late December 2021 and 0.8 mm in January 2022. February 2022 witnessed an average surface melt area of 1,702 km^2, indicating a reduction compared to the preceding month. This decline can be attributed to the significant decrease in the recorded average temperature, which ranged from –13.1 °C to –0.2 °C.

Overall, the austral summer of 2021-2022 demonstrated increased surface melting in December, as evidenced by the elevated average surface melt area during that period compared to other months.

5.3.4. Surface melt during the austral summer 2022-2023

During November 2022, there was a significant increase in surface melting, with an average surface melt area of 3,187 km^2. This represents a substantial rise compared to the previous November (2019, 2020, and 2021). The mean temperature during this period ranged from –10°C to –1.9°C. In December 2022, a reduction in surface melting was observed, influenced by precipitation and temperature changes. The average surface melt area was around 3,083 km^2, accompanied by snowfall during this period. The surface melt area decreased despite an increase in mean temperature from –4.9°C to 1.9°C, along with recorded precipitation of 0.3 mm. Thereafter, the average extent of surface melt amounted to 2,735 km^2 in January 2023, even during the peak melt season, despite an increase in temperature. The mean temperature varied from –3.2°C to 1.7°C. This reduced surface area experiencing melting could be attributed to the chilling effect of freezing katabatic winds (source: www.yr.no) experienced during this period. February 2023 witnessed an increase in the surface melt area, with an average surface melt of 3,725 km^2. The mean temperature ranged from –7.6°C to –0.5°C. The highest surface melting observed during this period aligns with the patterns observed in February 2020 and can be associated with the albedo effect.

The analysis of surface melt during the austral summers of 2019-2020, 2020-2021, 2021-2022, and 2022-2023 demonstrates distinct patterns and trends. The surface melt areas varied across the different years, with some years exhibiting higher melt extents compared to others. The influence of temperature fluctuations and precipitation on surface melt is evident, as they contribute to both the expansion and reduction of melt areas. Additionally, external factors such as freezing winds (Saunderson et al. 2022) and the albedo effect can influence the extent of surface melting.

5.4. Seasonal surface ice flow velocity

Temperature oscillations induce seasonal variations in the amount of surface meltwater on NIS, with increases in surface melt, area, and volume. However, as the melt season develops, a transition to a connected surface drainage network occurs, which allows for a gradual flow of surface meltwater toward the ice-shelf front (Friedl 2019). During the melt season, the area and volume of surface meltwater diminish near the grounding line and increase in the more distal northern regions of the ice shelf. The phase difference values obtained from the unwrapped interferogram are converted into ground displacement measurements in meters through the use of displacement maps. The line-of-sight displacement map provides information about the magnitude of movement either away from or towards the sensor (Negative values indicate movement in the direction away from the satellite along the radar line-of-sight, while positive values indicate movement towards the satellite along the radar line-of-sight).

The present study uses the vertical displacement which specifically calculates the component of the line-of-sight displacement, assuming that all deformation occurs in the vertical direction. These measurements were taken during the austral summers (NDJF) from 2019 to 2023. Figure 18 illustrates the unwrapped phase and displays the velocity map obtained for the datasets of January 10, 2023 (master) and January 22, 2023 (slave), for the purpose of representation. The displacement of NIS during each 12-day interval is measured, and this displacement is used to calculate the velocity for the corresponding 12-day period (Fig. 19). The surface ice flow velocity over NIS is analyzed for the study period in sections 5.4.1-5.4.4.

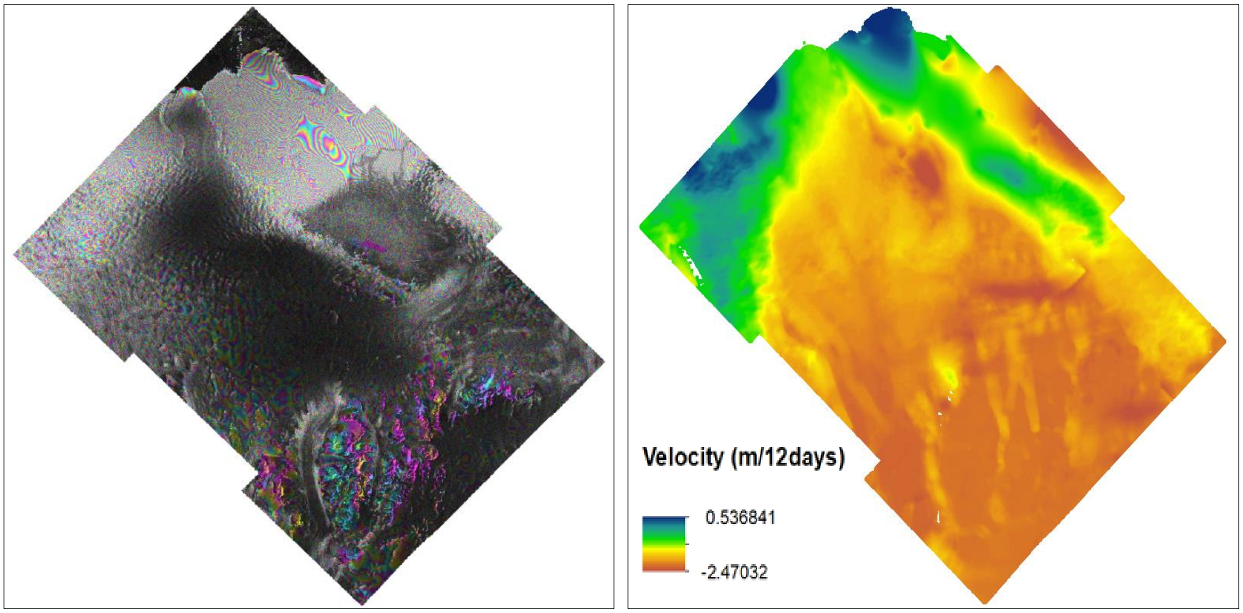

(a) (b)

Fig. 18. (a) The unwrapped phase and (b) surface ice flow velocity map obtained during January 10, 2023 (master) and January 22, 2023 (slave) over Dronning Maud Land

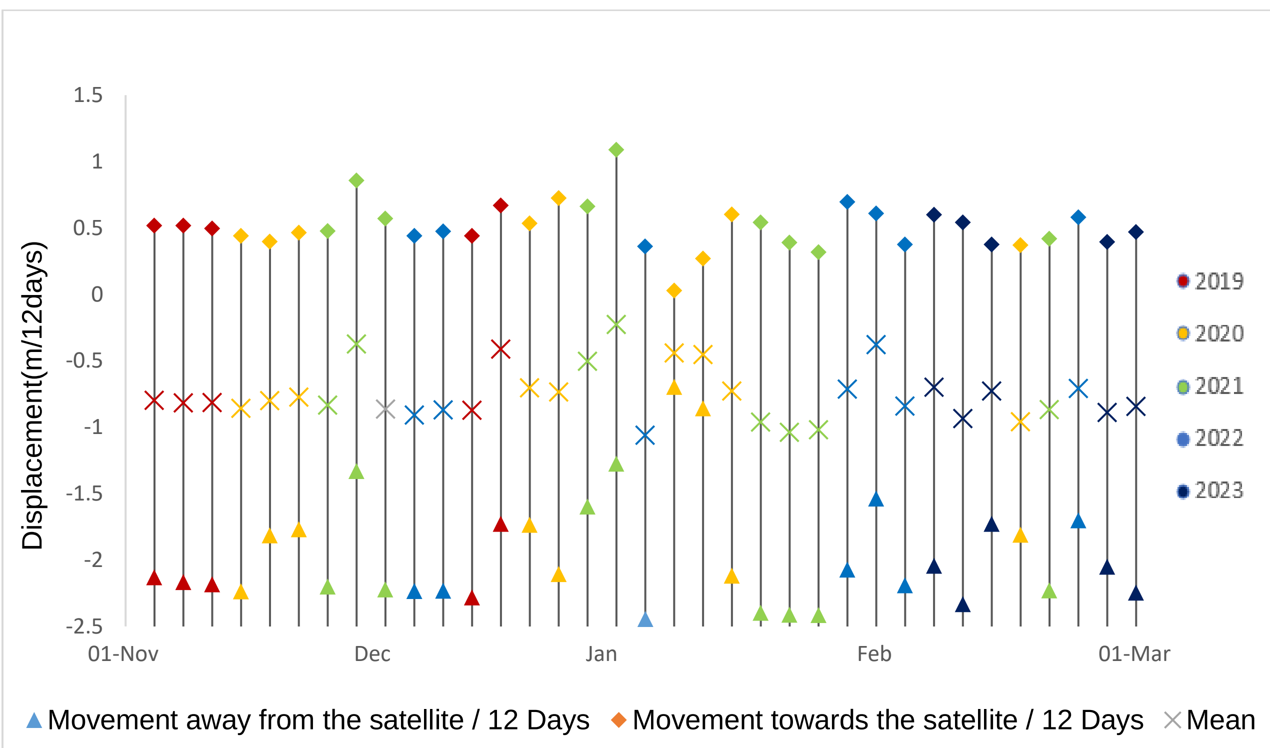

Fig. 19. The velocity obtained for 12-day time period during the months of austral summers considered for the study.

5.4.1. Ice velocity for the austral summer 2019-2020:

The data reveals a slight increase in velocity over time, with the measurement of 2.13 m/12 days in mid-November 2019 increasing to 2.18 m/12 days by the end of the month. This upward trend is further supported by the average velocity of 0.8 m/12 days during this period. However, a contrasting pattern emerges in December 2019, as the velocity experiences a decline from 2.28 m/12 days to 1.72 m/12 days. The mean velocity of 0.44 m/12 days recorded at the end of December 2019 suggests a deviation from the previous upward trend. Moving into January 2020, the velocity starts at 0.69 m/12 days but undergoes a substantial increase to 2.11 m/12 days by the end of the month. This significant rise signifies a surge in velocity, likely due to the peak melt season. During the early part of February to mid-February 2020, the mean velocity reaches its peak at 0.96 m/12 days. However, there is a subsequent decrease in the velocity values, dropping from 2.11 m/12 days to 1.81 m/12 days. When comparing the different time periods, it is interesting to note that the velocity observed in December 2019 surpasses that of November 2019, January, and February 2020.

5.4.2. Ice velocity for the austral summer 2020-2021

In November, the estimated surface melt area of approximately 1,519 km^2 remains comparable to the previous year, while the velocity experiences a decrease from 2.23 m/12 days to 1.81 m/12 days. This suggests a potential inverse correlation between surface melt and velocity. Moving into December, both the surface melt area decreases to around 1,239 km^2, and the velocity declines to 1.73 m/12 days. This indicates a possible positive correlation between the two variables. In January, the average extent of surface melt expands significantly to 2,474 km^2, corresponding to an increase in velocity from 1.73 m/12 days to 2.41 m/12 days. This suggests a potential positive correlation between surface melt and velocity during the peak melt season. However, in February, the average surface melt area decreases to 1,947 km^2, and the velocity also shows a decline from 2.41 m/12 days to 2.23 m/12 days. While both surface melt and velocity decrease, the relationship between the two becomes less clear. It is important to consider additional factors such as temperature fluctuations and wind effects that may influence the correlation between surface melt and velocity during the austral summer of 2020-2021.

5.4.3. Ice velocity for the austral summer 2021-2022

The data reveals a significant decline in velocity, from 2.20 m/12 days to 1.33 m/12 days, during the early November to end of November 2021 period. This sharp decrease indicates a notable change in the velocity values during that timeframe. However, in early December 2021, there is a rebound in velocity, reaching 2.22 m/12 days, with a mean velocity of 0.86 m/12 days. This indicates a temporary recovery from the previous decline. From mid-December to the end of December 2021, the velocity starts to decrease once again, reaching a value of 1.27 m/12 days, with a notably reduced mean velocity of 0.2m/12 days. This declining pattern suggests a continuation of the overall downward trend observed earlier. During the early January to mid-January 2022 period, there is an upswing in the mean velocity values, reaching their peak at 0.71 m/12 days. This period stands out as one of the relatively higher velocity values, possibly indicating a distinct phenomenon or contributing factor during that time. Subsequently, fluctuations in velocity (Halas et al. 2023) values are observed from mid-January 2022 to the end of February 2022, with values recorded at 1.53 m/12 days and 1.70 m/12 days, respectively. However, during this period, the mean velocity exhibits a decreasing trend, indicating a gradual decline in the overall velocity values.

5.4.4. Ice velocity for the austral summer 2022-2023

During mid-November 2022 to early December 2022, the velocity remains consistent at 2.23 m/12 days. However, there is a decrease in the mean velocity, declining from 0.9 m/12 days to 0.8 m/12 days. This indicates that while the overall velocity remains the same, there is a reduction in the average velocity during this period. Moving into mid-December 2022 to the end of December 2022, there is a noticeable decrease in velocity from 2.44 m/12 days to 2.19 m/12 days. The mean velocity also exhibits variations, ranging from 1.0 m/12 days to 0.8 m/12 days. These changes suggest a trend of decreasing velocity and highlight fluctuations in the average velocity values during this period. The maximum velocity experiences a decline from the end of December 2022 to the end of January 2023, with values decreasing from 2.42 m/12 days to 1.72 m/12 days. Additionally, the mean velocity shows variations, ranging from 0.9 m/12 days to 0.7 m/12 days. This indicates a decreasing pattern in both the maximum and average velocity during this timeframe. However, from early February 2023 to the end of February 2023, there is an increase in velocity from 2.05 m/12 days to 2.24 m/12 days. Interestingly, despite this increase, the mean velocity experiences a slight decrease, declining from 0.89 m/12 days to 0.84 m/12 days. These contrasting trends suggest a complex interplay between the maximum and mean velocity values. It is worth noting that the mid-December 2022 period during the austral summer 2022-2023 stands out with higher values of both maximum and mean velocity. This indicates a distinct period of increased velocity compared to other months of the study period.

These findings contribute to a better understanding of the relationship between surface melt and velocity over NIS. The data analysis consistently shows the higher maximum and mean velocity values occurring predominantly in January during the austral summers from 2019 to 2023. This suggests that January experiences the most significant melting, resulting in larger velocity measurements. This finding highlights the crucial role of surface melt in driving ice shelf velocity (Husman et al. 2022)(Banwell et al. 2019). Furthermore, the analysis demonstrates that December exhibits greater fluctuations in velocity compared to November, January, and February. This indicates a higher degree of variability and instability within the ice shelf during December, marking the onset of melting. The connection between velocity and basal melting is essential for understanding the dynamics of the ice shelf. This type of velocity fluctuation would lead to increased basal melting, causing the ice shelves to shrink instead of maintaining mass balance. These findings contribute to advancing our understanding of the intricate relationship between surface melt, velocity, and the behavior of NIS. They emphasize the significance of monitoring and comprehending these dynamics to assess the overall stability and future evolution of the ice shelf.

5.5 Seasonal surface Melt and surface ice flow velocity patterns during the austral summer 2019-2023

Velocity, which refers to the rate of ice movement, is a crucial parameter for understanding ice sheet dynamics and the impacts of climate change (Nagler et al. 2015). Surface melt, on the other hand, measures the extent of ice surface melting and serves as an important indicator of environmental conditions. By examining the relationship between velocity and surface melt, valuable insights can be gained into the complex interplay between ice dynamics and surface processes in Polar Regions. Analyzing the available data and studying trends in velocity and surface melt (figure 20) can uncover potential correlations and provide a deeper understanding of the dynamics of the studied region during the austral summer periods.

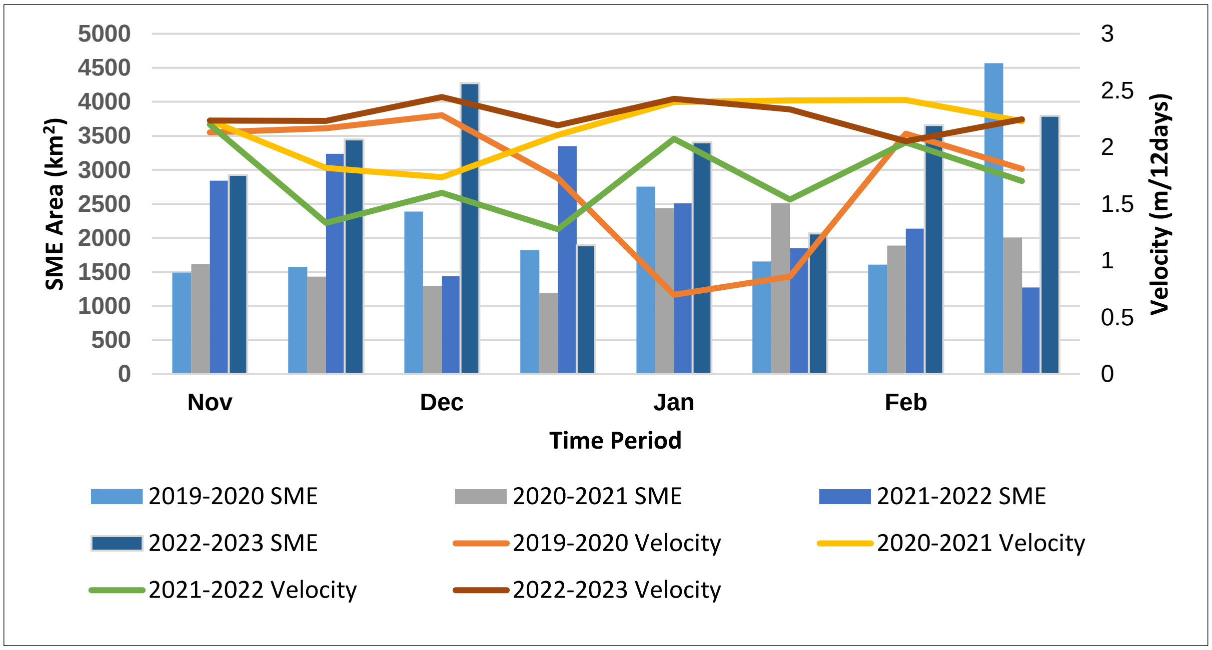

Fig. 20. SME versus the surface ice flow velocity for the austral summers 2019-2023.

5.5.1. Austral Summer 2019-2020

The surface melt area and velocity both rise in November 2019. While the velocity rises from 2.13 m/12 days to 2.18 m/12 days, the average surface melt area increases to 1,531 km^2. This implies a positive association between surface melt and velocity, showing that the tendency of ice velocity to rise as surface melting deepens. A striking contrast between surface melt and velocity can be seen in December 2019. The surface melt area expands further to 2,102 km^2, indicating a significant increase. However, the velocity experiences a decline from 2.28 m/12 days to 1.72 m/12 days. This suggests a possible decoupling or weakening of the correlation between surface melt and velocity during this period. For January 2020, both the surface melt area and velocity show a slight increase compared to December 2019. In addition to the velocity increasing from 1.72 m/12 days to 2.11 m/12 days, the surface melt area reaches 2,202 km^2. This shows that the positive relationship between surface melt and velocity has partially returned. The surface melt area and velocity both show a considerable increase in February 2020. 3,086 km^2 is a considerable increase in the surface melt area, and 2.11 m/12 days is the peak velocity.

This suggests that during February 2020, there is expected to be a significant positive association between surface melt and velocity. Overall, surface melt and velocity seem to be positively correlated, with minor variability and potential decoupling seen in December 2019. The positive correlation points to a potential feedback mechanism between surface melt and ice flow dynamics, showing that as the surface melt area rises, the ice velocity tends to increase as well.

5.5.2 Austral Summer 2020-2021

While the velocity decreases from 2.23 m/12 days to 1.81 m/12 days in November, the estimated surface melt area of 1,519 km^2 is similar to that in the previous year. This shows that surface melt and velocity may be inversely correlated. In December, both the surface melt area and the velocity both fall to 1.73 m/12 days, or around 1,239 km^2. This suggests that there may be a positive association between the two factors. An increase in velocity from 1.73 m/12 days to 2.41 m/12 days causes the average surface melt extent to dramatically increase in January to 2,474 km^2. This shows that during the peak melt season, there may be a positive link between surface melt and velocity. However, in February, both the average surface melt area and the velocity both fall to 1,947 km^2 and 2,23 km^2, respectively. Surface melt and velocity both drop, although there is less of a link between the two. It is crucial to take into account any other elements that may affect the link between surface melt and velocity during the austral summer of 2020–2021, such as temperature swings and wind effects.

5.5.3. Austral Summer 2021-2022

The average area of the surface melting in November 2021 rises to 1,618 km^2, while the velocity falls from 2.20 m/day to 1.33 m/day. This shows that surface melt and velocity may be inversely correlated. By December 2021, the surface melt has increased to a size of around 2,392 km^2, and its pace has rebounded to 2.22 m/day. This suggests a small increase in velocity. Despite being the peak melt season, in January 2022, the surface melt area falls to 2,177 km^2 as the velocity fluctuates. Precipitation may have an impact on the lowered surface melt, and the velocity values may change as a result of other variables. The surface melt area falls to 1,702 km^2 in February 2022, and the velocity is still erratic. According to the analysis, there will likely be a complicated interaction between surface melt and velocity during the austral summer of 2021–2022, depending on a number of variables including temperature, precipitation, and other external pressures.

5.5.4. Austral Summer 2022-2023

While the velocity remains constant at 2.23 m/12 days in November 2022, there is a noticeable rise in surface melting, with an average surface melt area of 3,187 square kilometres. This shows that surface melt and velocity may be positively correlated. However, even when the surface melt area drops to 3,083 km^2 in December 2022, the velocity decreases. This suggests that the positive association shown in November may be waning. The surface melt area falls to 2,735 km^2 in January 2023, while the velocity shows changes, showing the complex relationship between the two variables. A rise in surface melt area (3,725 km^2) and velocity in February 2023 may indicate that the positive link has been restored. The analysis predicts that surface melt and velocity will interact dynamically throughout the austral summer of 2022–2023, depending on a variety of variables including temperature, precipitation, and wind patterns.

Overall, different austral summer periods resulted in different relationships between surface melt and displacement. While certain favourable correlations (such as November 2019 and February 2023) were identified, there were also instances of weak correlation or dissociation (such as December 2019 and January 2021). The observed fluctuations may be influenced by additional elements such as wind patterns, precipitation, and specific local conditions. The relationship between surface melt and displacement would be better understood with additional research and consideration of these variables. In fact, the analysis and interpretation of the link between surface melt and displacement might be impacted by data gaps and the frequency of data collection. Higher revisit durations, which refer to longer gaps between data acquisitions, may result in incomplete or missing data, which could leave gaps in the dataset. The capacity to record short-term fluctuations and accurate correlations between surface melt and displacement may be hampered by data gaps. The lack of data during particular time periods could cause crucial events or developments to go unnoticed. The dynamics and interactions between surface melt and displacement may not be accurately captured by the analysis as a result. It is imperative to enhance data gathering techniques and raise observational frequency in order to lessen the effects of data gaps. More thorough and continuous datasets can be produced by using satellite imagery with higher revisit rates or by combining other remote sensing techniques. Additionally, incorporating field observations and measurements taken on the ground can improve the analysis's precision and dependability. It is feasible to gain a more thorough understanding of the relationship between surface melt and displacement, enabling more reliable interpretations and correlations, by minimizing data gaps and enhancing data coverage.

5.6 Dynamics of ice flow in melt and non-melt regions of NIS: Velocity Insights from Profiles R1-R4

When the maximum temperatures rise, the area and volume of surface water bodies expand, merge with nearby water bodies, and form new extended networks of surface water. The surface melt is transmitted to the ice shelf's front and over the southern region, despite the fact that surface water bodies are predominantly concentrated along NIS's grounding line. Large, round, and linear water bodies are likely aided in creation by the ice-shelf surface's architecture. The large, encompassing entities that contain and transport the surface meltwater across the ice shelf to distant places are reported to undergo a lateral migration of water throughout the melt season from the small, isolated bodies close to the grounding line. This technique of surface lake overtopping, which forms shallow channels linking water bodies and aids in the flow of water to the ice shelf front, may be responsible for this lateral water transfer (Banwell et al. 2019).

Early in the melt season, surface meltwater on NIS ponds forms small surface lakes at Schirmacher Oasis in reasonably level regions near the grounding line. As a result, the velocity pattern analysis at the melt and non-melt parts of NIS will provide more information about the four linear profiles R1, R2, R3, and R4 that were chosen to span NIS and have a length of 30 km each (figure 21). R1 and R2 stand for the ice shelf's melt regions, whereas R3 and R4 are the ice shelf's non-melt regions, respectively. These profiles were depicted in a bottom-to-top arrangement. Melt is observed in the northwest (ice front) and southern part (grounding line) of the shelf above the Schirmacher Oasis, whereas, in contrast, the central part of the shelf remains largely unaffected by melting during most of the melt seasons. For the austral summer of 2019–2023, the ice flow velocity findings from on-demand SAR data processing across surface melt and non-melt regions are evaluated in relation to the distance for the maximum and minimum surface melt periods of 2019-2023 austral summers.

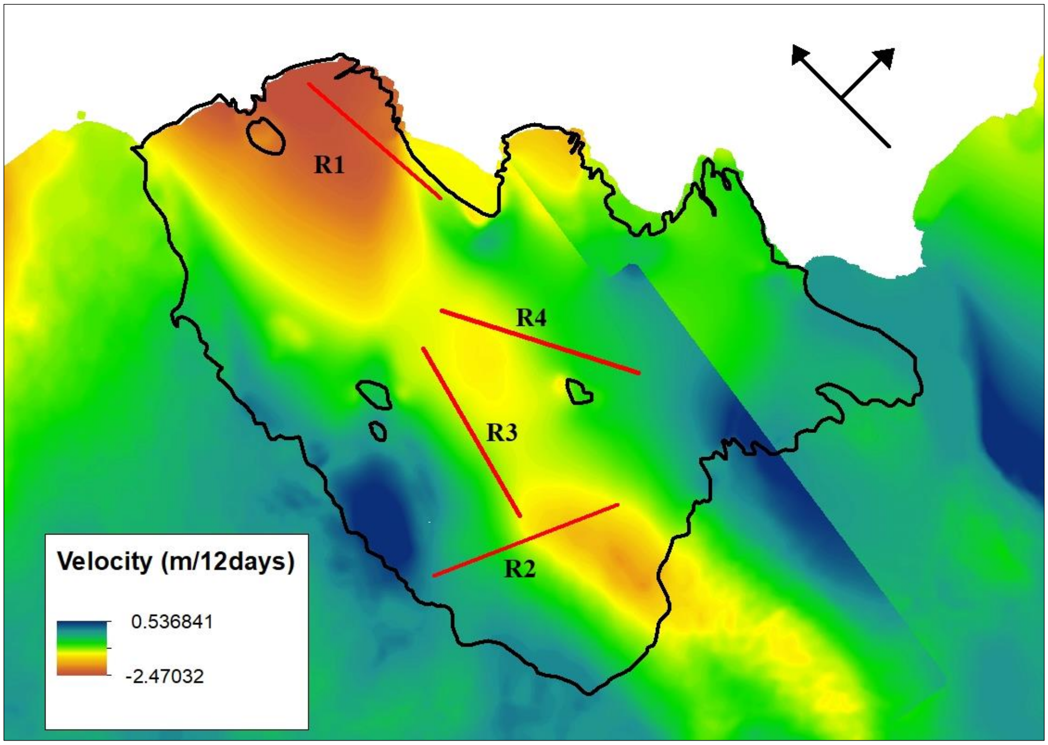

Fig. 21. The four profiles R1, R2, R3, and R4 of 30-km long drawn over NIS in the melt and non-melt regions (Background image is surface ice flow velocity map estimated during January 2023)

5.6.1 Profile R1: melt region

Profile R1, located in the melt region on the northwest side of NIS (Figure 21), was analyzed for the minimum and maximum Surface Melt Extent (SME) periods between AS 2019-2023 as given in figure 22. The ice flow pattern remained constant, averaging 0.35 m/12 days, during the lowest and maximum SME period of austral summer 2021–2022. In contrast, between the lowest and maximum SME periods in the austral summer of 2020–2021, the velocity rose on average by twice as much, from 0.9 m/12 days to 1.8 m/12 days. In contrast, the velocity increased on average twice as much during the minimum and maximum SME in the austral summer of 2020–2021, from 0.9 m/12 days to 1.8 m/12 days. However, a diminishing tendency in velocity was evident in the minimum and maximum SME periods in the austral summers of 2019–2020 and 2022–2023, with an average velocity of 1.5 m/12 days. Additionally, it was noted that the velocity gradually increased beyond a distance of 10 km, which was probably caused by a steady decline in the slope towards the ice/calving front. This initial 10 km distance was accompanied by an ice rise/rumple feature at the ice front, which had the effect of buttressing the ice flow.

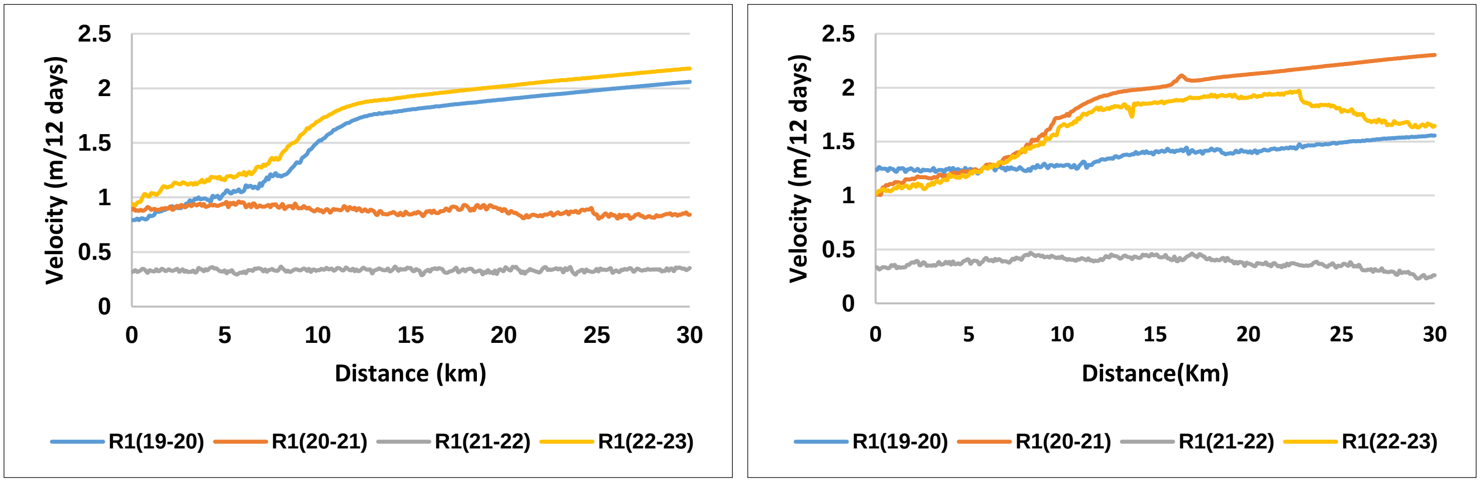

(a) (b)

Fig. 22. Profile R1 drawn over a melt region during (a) minimum surface melt and (b) maximum surface melt periods during austral summers of 2019-2023

5.6.2. Profile R2: melt region

On the southern end of the NIS, at the grounding line above the Schirmacher Oasis (as shown in Figure 21), the profile R2 was examined and given in figure 23. Over the AS 2019–2022, 2020–2021, and 2022–2023 periods, similar velocity patterns were seen, with an average and maximum ice flow of roughly 1 m/12 days and 1.4 m/days, respectively. However, compared to past austral summers, AS 2021–2022 had a notable reduction in profile R2's velocity pattern of almost double the size. High ice flow velocity found close to the grounding line supports the possibility of melt ponds there. Overall, a decrease in ice flow was seen as the distance increased up to 15 km, either as a result of less melting or the lack of water bodies in the profiled region. Only linear water bodies were seen on the sidewalls of the R2 profile after 15 km, which suggests that the ice flow has decreased and there is less melt water available.

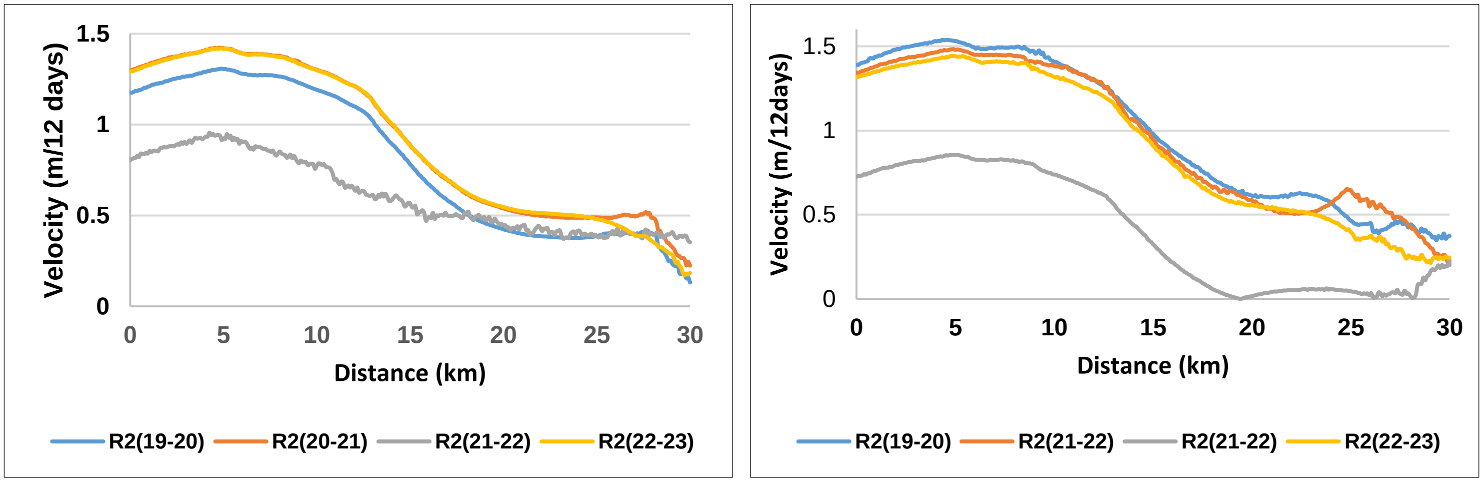

(a) (b)

Fig. 23. Profile R2 drawn over a melt region during (a) minimum surface melt and (b) maximum surface melt periods during austral summers of 2019-2023

5.6.3. Profile R3 & R4: non-melt region

In the central part of NIS, specifically above the Schirmacheroasen, non-melt regions R3 and R4 were identified. The velocity profiles during the minimum and maximum SME periods of the austral summer of 2019-2023, as depicted in Figure 24, provide insights into the behavior of ice flow in these regions. For both R3 and R4, a consistent pattern of velocity was observed during the austral summer of 2019-2020, with the average and maximum velocities ranging from 0.9m to 1 m/12 days and 1.1 to 1.3 m/12 days, respectively, exhibiting negligible variations. This similar velocity pattern persisted during the austral summer of 2020-2021 and 2022-2023, maintaining an average velocity of 1 m/12 days.

However, during the austral summer of 2021-2022, a slight increase in the maximum velocity was noted, ranging from 0.4 to 0.56 m/12 days, while the average velocity remained constant at 0.3 m/12 days. This indicates a relatively stable flow with only a minor variation in maximum velocity during that specific period. Overall, an overall steady increase in velocity with distance was observed, signifying the influence of a gradual decrease in slope towards the ocean. Remarkably, in the non-melt regions of R3 and R4, the velocity exhibited a relatively constant behavior throughout the austral summer periods examined in this study.

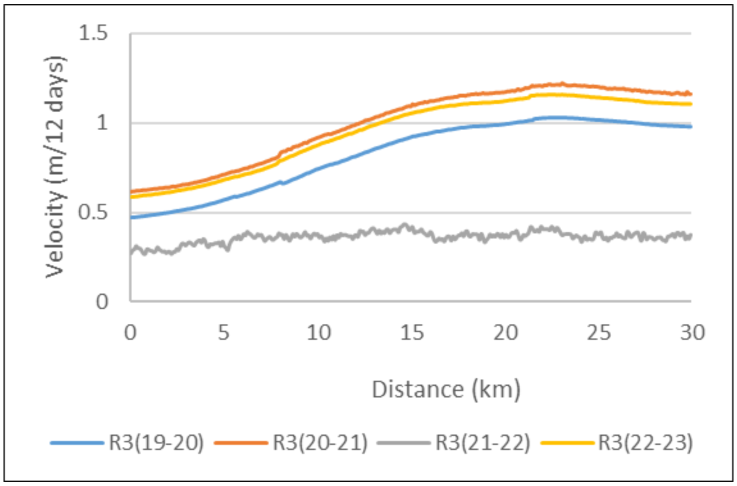

(a)

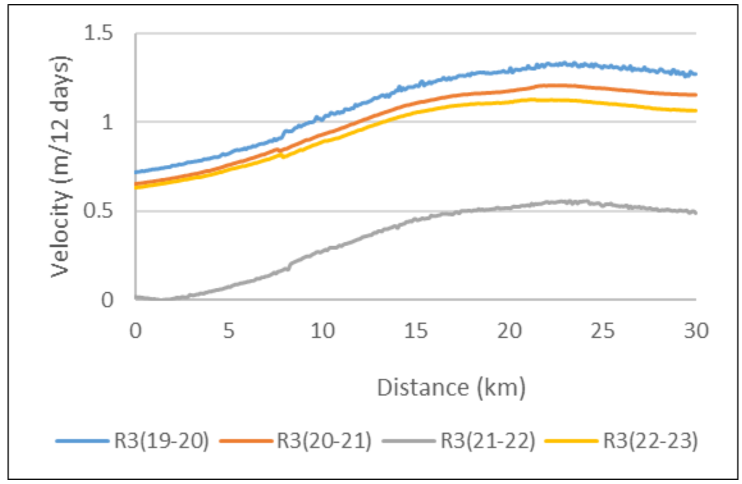

(b)

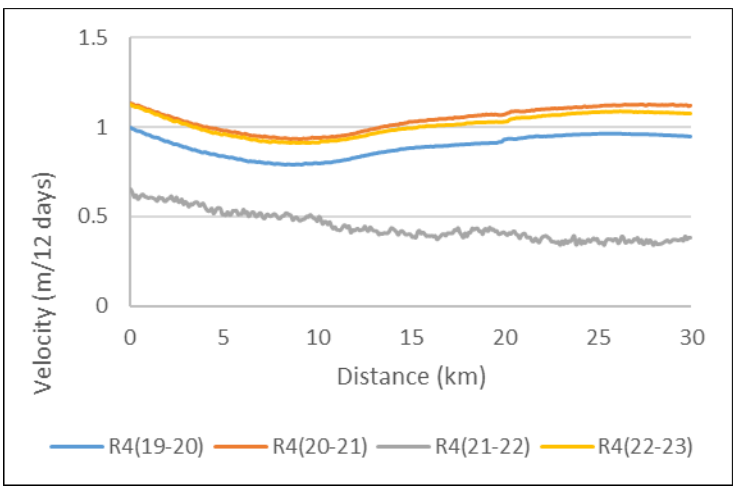

(c)

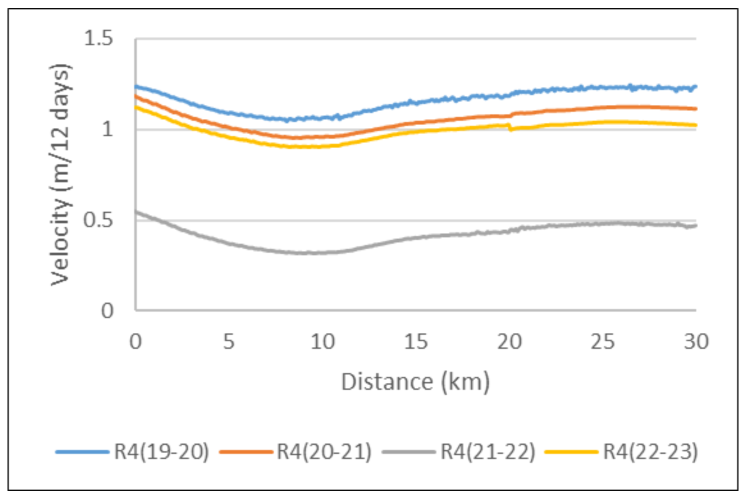

(d)

Fig.24. Profile R3 & R4 drawn over the non-melt regions during austral summers of 2019-2023 (a) R3 in minimum surface melt period, and (b) R3 in maximum surface melt period (c) R4 in minimum surface melt period, and (d) R4 in maximum surface melt period

5.7. **Field Validation**

The fieldwork was conducted during the austral summer period of 2022-2023 as a part of the 42nd Indian scientific expedition to Antarctica. During the fieldwork, a melt pond (figure 25) was considered near the Maitri, Indian research base (due to logistical feasibility) located at (11°45'6.786"E, 70°46'22.475"S) in Dronning Maud Land, East Antarctica for installation of Pressure Sensor Assembly (PSA)(Fausto et al. 2012). Due to the unavailability of cloud-free satellite-based optical data over the selected melt pond, Unmanned Aerial Survey was carried out over the selected melt pond using P4 multispectral sensor. Details about the pressure sensor and UAV sensor used are given in Table 4.

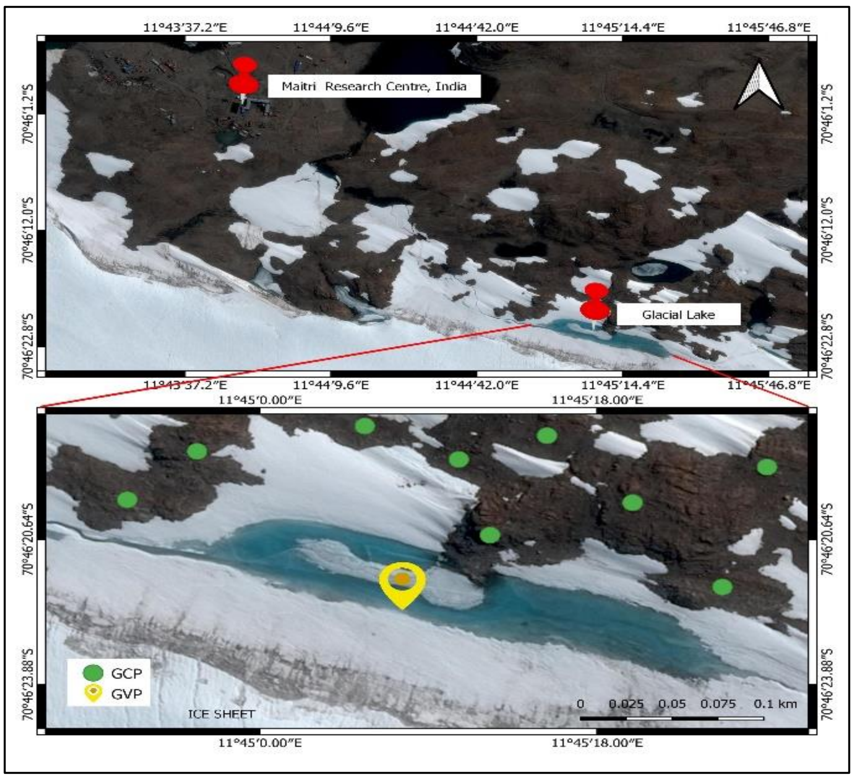

Fig. 25. Validation site: Glacial Lake / melt pond selected near the Maitri, Indian research station located in Dronning Maud land, East Antarctica.

Table 4 Details about the sensor used for field validation i.e., pressure sensor for depth estimation (equivalent water level) and a multispectral sensor for estimating the depth over the melt pond using MPD model

Instrument type	Manufacturer	Model type	Accuracy
Pressure sensor	KELLER Druckmesstechnik AG, Switzerland	DCX-22 SG	±2. 5 (cm)
Multispectral sensor	SZ DJI Technology Co Ltd (DJI), China	P4 Multispectral	Wavelength accuracy of ±1 nm

5.7.1. UAV with P4 Multispectral sensor:

The P4 RTK (real-time kinematic) Multispectral is a high-precision UAV that is equipped with a multispectral camera as shown in figure 26. This sensor allows the UAV to capture images of the study area in multiple spectral bands. The P4 Multispectral has six 1/2.9-inch CMOS sensors, including one RGB sensor for visible light imaging and five monochrome sensors (Blue (B): 450 nm; Green (G): 560 nm; Red (R): 650 nm; Red edge (RE): 730 nm; Near-infrared (NIR): 840 nm) for multispectral imaging. The RGB sensor has an effective pixel count of 2.08 MP, and the five monochrome sensors each have an effective pixel count of 2.08 MP. The P4 Multispectral can be used to collect valuable data about the earth's surface, such as crop health, forest health, and environmental conditions. The present study attempts to showcase the ability of using UAV data for cryosphere studies in Antarctica.

Fig. 26. The UAV survey over the glacial lake with P4 multispectral sensor

5.7.2. Pressure Sensor Assembly (PSA):

The PSA's current design is given in graphical representation as shown in figure 27. An armored silicon hose of 26mm diameter with a total length of 10m that houses a pressure sensor was used. The pressure sensor is attached to a 23-cm long, slightly larger than 26 mm iron rod that is inserted with silicone sealant and connected with hose clamps in the bottom half of the hose. The rod serves as both a waterproof closure and a dead weight. A T-junction is fitted at the top end of the hose to allow the logger cable exiting the closed PSA system to link the pressure sensor to the logger. The other T-junction branch connects to a 2L expansion rubber bladder. The bladder is generally half-full to enable volume variations in the antifreeze (for example, due to sun heating) without causing pressure buildup in the assembly. The hose is filled with an antifreeze solution (ethylene glycol with water in the proportion 50:50) and the PSA was mounted on a pole of 5-m long erected in the pond/lake area with the help of a Teflon pulley and guides. The pulley arrangement is made to ensure that the pressure sensor slides down as the melting progress and remains in contact with the pond ice floor /bottom bed surface over which meltwater is ponding.

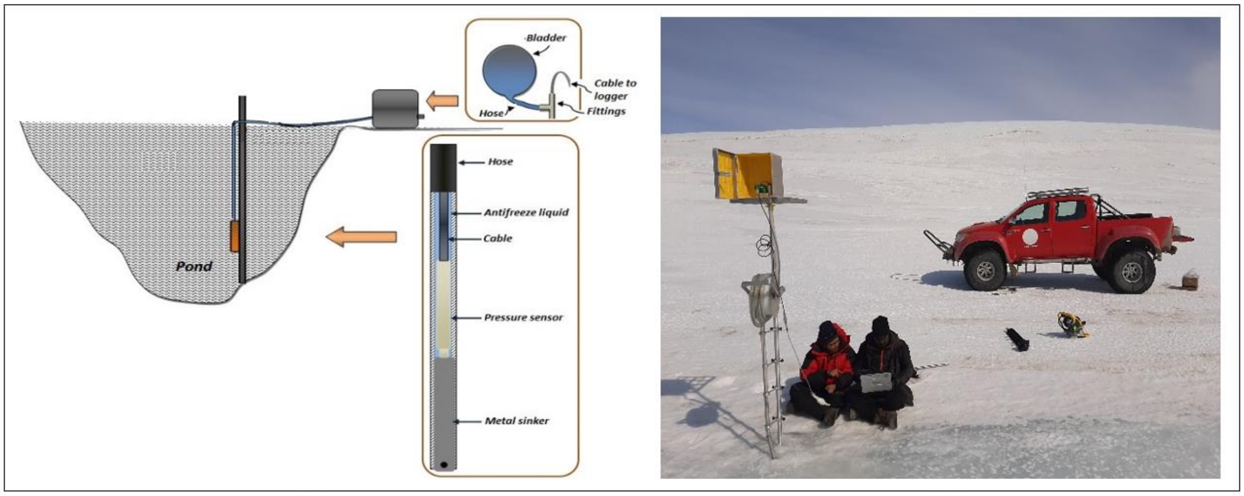

(a) (b)

Fig. 27. (a) The graphical representation of the Pressure Sensor Assembly installation over the melt pond selected for the study (b) The bladder box on the T-junction is fitted at the top end of the hose to allow the logger cable exiting the closed PSA system and other T-junction's branch connects to a 2L expansion rubber bladder

The setup was installed by drilling up to 3 m into the frozen pond (location) with a Jiffy ice auger (4G four stroke) and extenders by late November 2022 before melting. The sensor used is a DCX-22 data logger which is a versatile device designed for measuring water level, water pressure, and temperature. The Sealed Gauge variant delivers the highest level of accuracy and is well-suited for submersion applications. With an extended battery life, the DCX-22 data logger can record data for up to 10 years, capturing measurements at hourly intervals.

5.7.3. PSA data collection:

The pressure sensor was programmed to collect pressure and temperature data for every 15 minutes with the help of the data logger attached to the sensor. Data gaps were encountered when the sensor was exposed due to refreezing of pond / low water levels post-late December 2022. Data was retrieved from the data logger on a daily basis to avoid data loss due to low battery/memory and also to ensure that the sensor bottom is always in contact with the melt pond ice floor/bottom bed surface. In the present study, the melt pond/SGL depth is defined as the vertical distance between the water level and the lowest point of the melt pond/SGL bed within the cross-section of the melt pond/SGL. The mean temperature and pressure from the melt pond bottom as measured by the sensor during the field period are shown in figure 28.

The hydrostatic pressure of a fluid in the bar is measured and stored by the DCX-22 device. The conversion of pressure from bar to water column level in meters of water (mH2O) is significantly affected by the density of the medium. The KOLIBRI Desktop software (Leitner et al. 2013) utilizes equation (5) to calculate the height of the water column. A water density of 999.89 kg/m^3 is considered as the average temperature on 20th December 2022 was found to be around 1°C. The iron rod length has been compensated for the depth estimates.

$$d = \frac{P}{\rho * g} \tag{5}$$

where P = hydrostatic pressure (N/m^2), ρ = water density (kg/m^3), g = gravitational acceleration (m/s^2), d = height of water column (m)

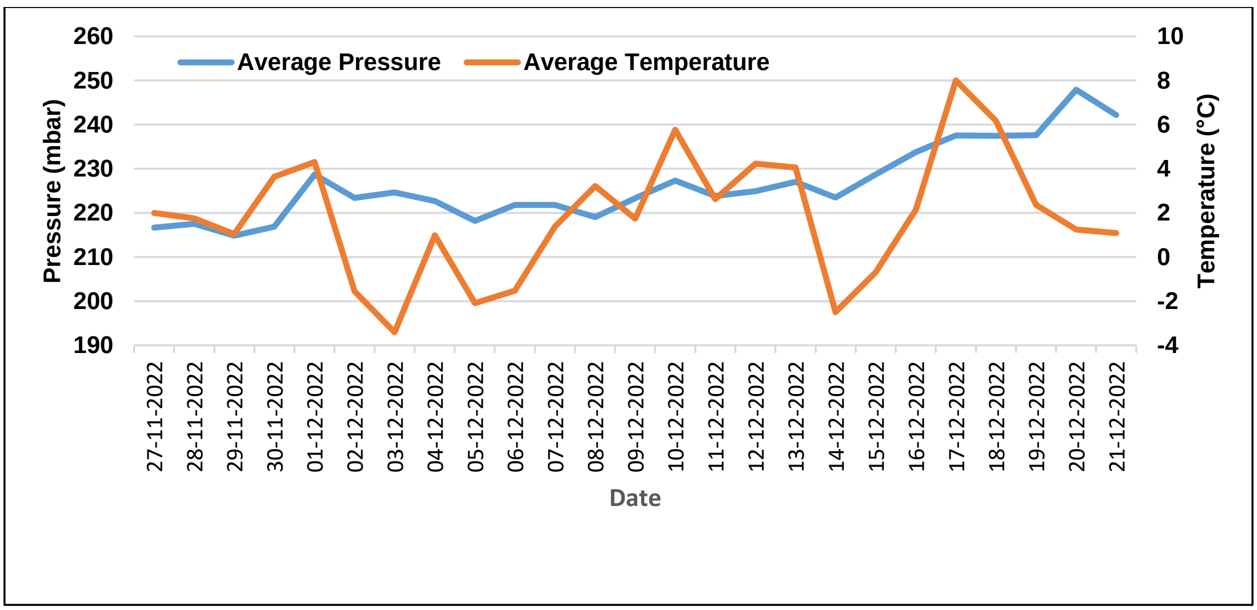

Fig. 28. Average pressure and temperature obtained from the pressure sensor installed on the selected glacial lake/ melt pond for 25 days during the austral summer 2022-2023

5.7.4. GCPs and GVPs

The ground control points (GCPs) were established on the field (figure 29) using printed white crosses over the stable regions and the melt pond to achieve high positional accuracies and to minimize elevation-dependent biases. The GCP survey was carried out using SP80 Spectra Precision GNSS receivers. Manual measurements of pond depth were also carried out at different points spread across the pond's periphery. The PSA installation was aimed at depth measurement interior to the melt pond where manual interventions were not feasible as the melt progresses (presence of slush, wide melt channels, etc.). The PSA installed point and manual measurement points were also surveyed as ground validation points (GVPs).

(a) (b)

Fig.29. (a) Manual measurement of the depth over selected melt pond at different locations for (b) The PSA setup installed at the site with the GVP i.e., location of the setup (using printed white crosses)

.

5.7.5. Melt pond depth estimation

The radiative transfer model was employed to estimate the depth of the melt pond using multispectral data collected from UAV (Tovar-Sánchez et al. 2021 and Archibold et al. 2015). The estimated depth profile is presented in Figure 30. The model-based results were compared with measurements obtained through PSA and manual measurements. The comparison is summarized in Table 5. Variations in the recorded depths of melt ponds arise from uncertainties and the discrepancy in timing between measurements and aerial surveys conducted at various intervals throughout the observation day. Figure 30 illustrates the regression analysis conducted to compare the field-based depth measurements with the model-based results. The Pearson's correlation coefficient of 0.9 indicates a strong linear positive correlation between the two datasets. The comparison was performed by calculating the root-mean-square error (RMSE) between the physical in-situ measurements obtained at the field points and the results derived from the model.

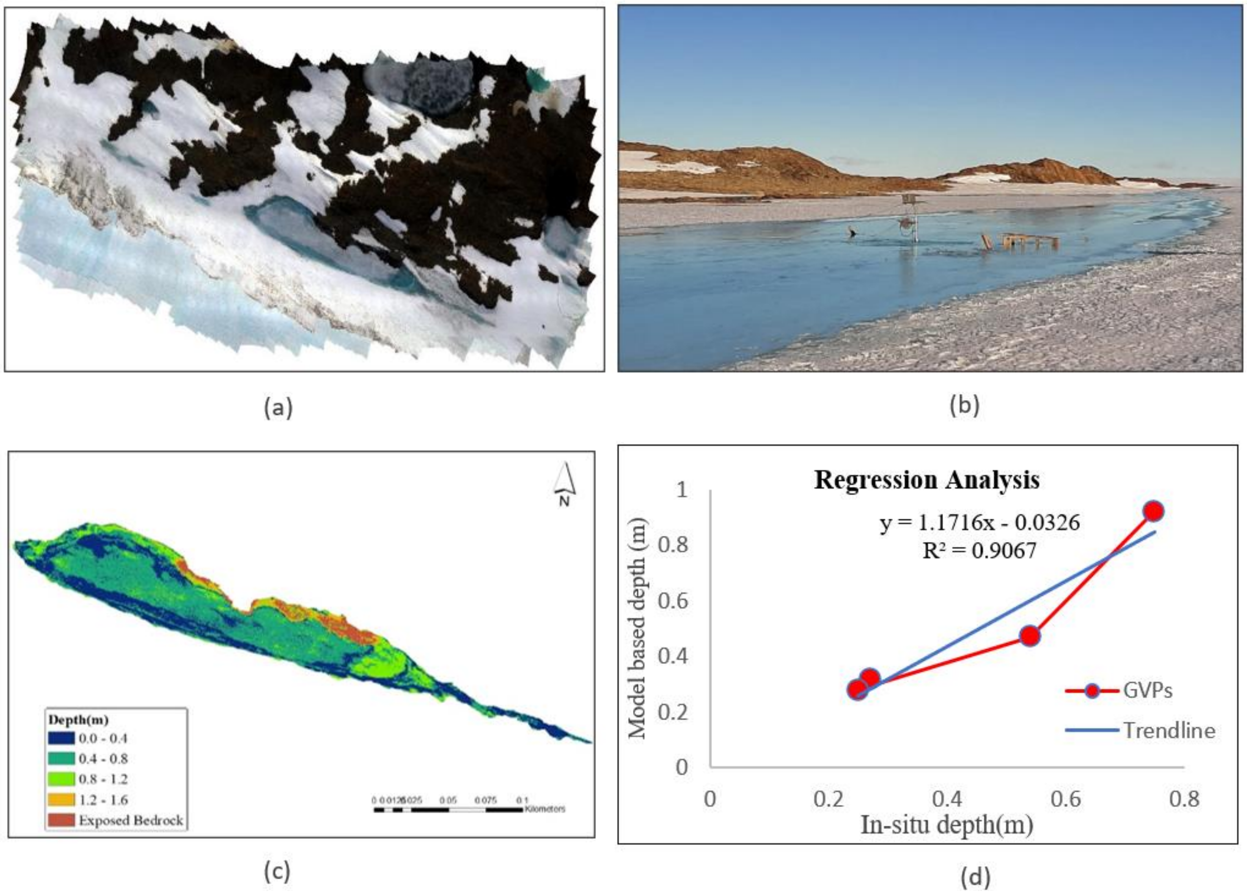

Fig. 30. (a) An aerial view of the selected melt pond, the RGB image of the lake obtained from P4 multispectral sensor, (b) The view of the lake during the peak melting period, on 20th December 2022, (c) The model-based melt pond depth derived from the UAV survey on 20th December 2022, (d) Correlation analysis of the measured values

Table 5 Depth values obtained from the pressure sensor and Melt Pond depth model for 20th December 2022

Parameters	**Findings**
Date of validation / UAV survey data	20th December 2022
Model-based depth at GVP	0.75 ± 0.2m
PSA-based depth at GVP	0.92 ± 0.03 m
RMSE at GVP	0.17

5.7.6. Limitations

The present study analyzed the surface melt NIS which is 130 m wide and 80 m long (Dell et al. 2020) with a large number of melt ponds and SGLs. The parameters studied are highly dynamic and varied in temporal and spatial evolution (Zhu et al. 2023). The depth estimation over NIS was limited only to the spatial extent from 70.3823°S, 10.3667°E to 76.7242°S, 12.8838°E. This study is confined to the surface melt in the form of melt ponds and SGLs during the period from 2000 to 2023. Various factors such as (a) large or small debris slumps, (b) ice calving, (c) katabatic wind effect, (d) pond floor collapse, (e) subaqueous melt, (f) structural collapse and (g) variations in water storage caused by a changing balance between water filling (melting) and drainage (discharge) are not considered in in detecting the changes in pond/lake water level. These factors can all contribute to changes in water level, and by analyzing the data, scientists can better understand the causes of these changes and the potential impacts on the environment. Due to logistical constraints, the installation was done at only one melt pond location. The PSA data is used only to validate the model-based melt pond depth estimation in addition to manual depth estimations.

5.7.7. Calibration:

Users have the capability to calibrate the pressure sensors integrated into the DCX logger unit. The calibration process is performed using the KOLIBRI Desktop software. During the calibration procedure, it is crucial to ensure that the sensors are checked or calibrated in the same positions they occupy in the measuring point, typically in an upright position. Additionally, the sensors should be positioned adjacent to each other at the same level. It may be necessary to recalibrate these sensors in various situations, such as after maintenance work, when altering the measurement setup, or after the measuring station has been operational for a year or longer. Before the UAV survey, calibration of the IMU, compass, and camera/sensor were carried out as per the operations manual.

5.8. Field-based ice flow motion

Due to logistical feasibility, field validation of ice flow was conducted using SP80 Spectra Precision GNSS receivers. Two ground control points (GCPs) were established near the grounding line of the NIS during 29th December 2022 to 10th January 2023, with a 12-day interval (Figure 31). This data collection timeframe was synchronized with Sentinel-1 satellite data acquisition. The survey was carried out in static mode, and post-processing of the base-related data was conducted. The obtained displacement values from both the GNSS and DInSAR processes for the NIS are presented in Table 6. It is important to note that uncertainties exist, and discrepancies in the measured displacements are observed due to the different nature of the measurements. The GNSS-based displacement provides a 3D measurement, while the DInSAR-based measurement is in the Line of Sight (LOS) direction (Komac et al. 2015). These differences, along with uncertainties, contribute to the observed variations in the measured displacements (Figure 32).

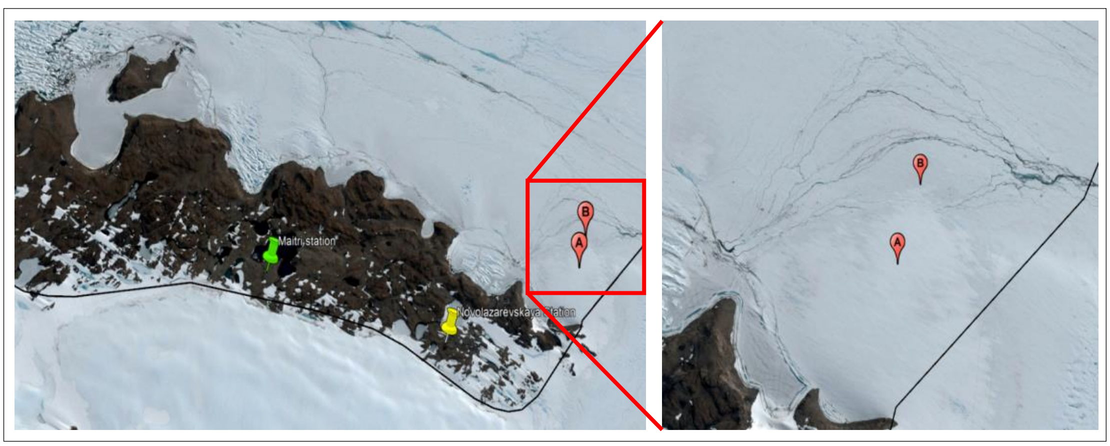

Fig. 31. Location of two ground control points (GCPs) near the grounding line of the NIS during the period of 29th December 2022 to 10th January 2023, with a 12-day interval.

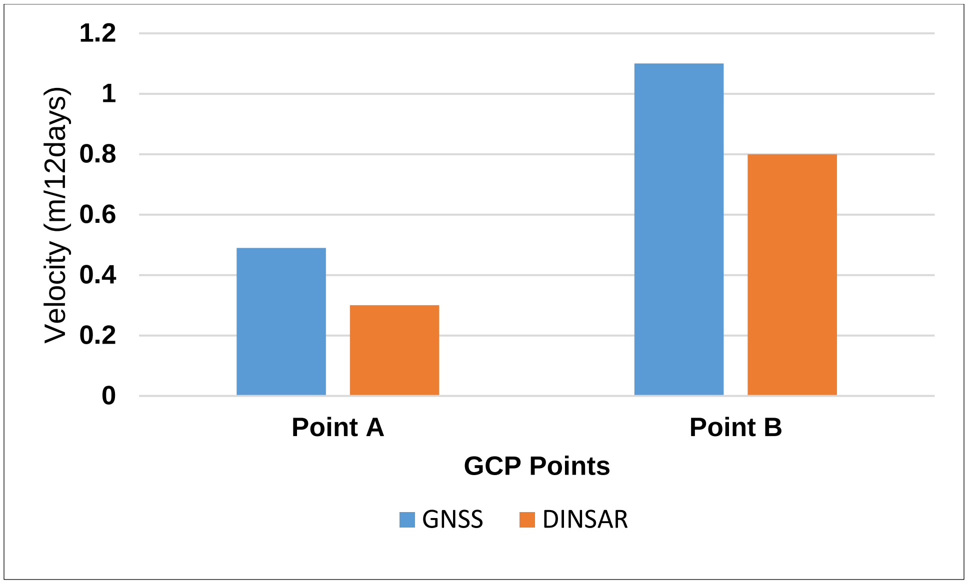

Fig. 32. The velocity (m/12days) recorded using GNSS and DInSAR at the GCP points point A and B during the period of 29th December 2022 to 10th January 2023.

5.8.1 Uncertainty in surface ice flow velocity:

In regions adjacent to the NIS that are considered stable (Schirmacher Oasis), a buffer of three pixels (equivalent to approximately 90 m) was applied to compare ice and ice-free zones. Utilizing nearly 200 samples, the Root Mean Square Deviation (RMSD) was found to be approximately 2.8 m/year. It is important to note that the accuracy of these measurements is influenced by the level of coherence observed between the SAR images used. A higher degree of coherence is achieved when employing a smaller temporal resolution and a perpendicular baseline, leading to improved accuracy in the measurements obtained.

6. Conclusion

An extensive analysis of NIS, East Antarctica was conducted, focusing on SGL parameters, seasonal surface melt extent, and surface ice flow velocity. Incessant monitoring of meltwater is essential to assess the possibility of ice shelf destabilization. SGL depth and area have increased relative to the year 2000, and this has been followed by an increase in volume. According to the decadal scale, between January 2003 and January 2023, the depth and volume of melt ponds grew by a factor of 1.5 while the area increased by a scale factor of 1.2. While SGL development is minimal in the middle of the ice shelf, surface lakes are frequently found in the interior regions of the ice shelf. These cyclical variations in the total lake area cause oscillations in meltwater volume during the melt season. With limited data, the seasonal surface melts and ice flow velocity fluctuations of the NIS were predicted and analysed with a focus on the austral summers of 2019–2023. The dynamics of ice flow in melt and non-melt portions of NIS are shown by the velocity insights from profiles R1–R4. The Schirmacher Oasis shelf's northwest (ice front) and southern (grounding line) regions have experienced melt, but the shelf's middle portion has remained dry for the most of these melt seasons. This indicates a relatively stable flow with only a minor variation in maximum velocity during that specific period. Overall, there was a consistent increase in velocity with distance, indicating the influence of a gradual decrease in a slope towards the ocean with the analyzed error of 2.8 m/year. The satellite-based results are field validated during the 42nd Indian Scientific Expedition to Antarctica using a UAV-based aerial survey, pressure sensor Assembly based dataset, and GNSS survey. The findings of this study give essential data for assessing NIS's sensitivity to climate change and defining future estimates on sea level rise, specifically surface melting, melt ponds/SGLs, and its impact on ice flow velocity. Overall, the impact of meltwater on an ice shelf is determined by the amount and distribution of the water, as well as the ice shelf's overall state and stability. With climate change causing unprecedented melting of polar ice, scientists and policymakers are becoming increasingly concerned about the effects of meltwater on ice shelves. This suggests that significant increases in SGL coverage and volume should be anticipated under enhanced atmospheric warming, suggesting that SGLs are likely to grow in the ice-shelf regions susceptible to hydro fracture.

Declaration of competing interest

The authors declare that they have no known competing financial interests or personal relationships that could have appeared to influence the work reported in this paper.

Data availability

Data will be made available on request.

Acknowledgement

The authors acknowledge the logistical support given by the National Centre for Polar and Ocean Research, Ministry of Earth Sciences, Govt. of India under the Indian Scientific Expedition to Antarctica (ISEA) with project code 42-AMOS/OR-06(2) to undertake this research. The authors gratefully acknowledge the support rendered by PTICL, MM Forgings, TATA STEEL, Jyothy Industries, Rational Technologies and CIIRC, Jyothy Institute of Technology, Bengaluru.

References

1. Alimasi N, Enomoto H, Hirasawa N. 2020. Spatiotemporal variation of ice sheet melting in the Antarctic coastal marginal zone and the influence of ice lenses and rain using satellite microwave observation. Polar Sci [Internet]. 25(July):100561. https://doi.org/10.1016/j.polar.2020.100561
2. Alley, K. E. Studies of Antarctic Ice Shelf Stability: Surface Melting, Basal Melting, and Ice Flow Dynamics, PhD thesis, Department of Geological Sciences, University of Colorado Boulder, 2017.
3. Alley KE, Scambos TA, Miller JZ, Long DG, MacFerrin M. 2018. Quantifying vulnerability of Antarctic ice shelves to hydrofracture using microwave scattering properties. Remote Sens Environ. 210(January):297–306. https://doi.org/10.1016/j.rse.2018.03.025
4. Aoki, S., Takahashi, T., Yamazaki, K. et al. Warm surface waters increase Antarctic ice shelf melt and delay dense water formation. Commun Earth Environ 3, 142 (2022). https://doi.org/10.1038/s43247-022-00456-z
5. Archibold AR, Rahman MM, Yogi Goswami D, Stefanakos EK. 2015. The effects of radiative heat transfer during the melting process of a high temperature phase change material confined in a spherical shell. Appl Energy. 138:675–684. https://doi.org/10.1016/j.apenergy.2014.10.086
6. Arthur JF, Stokes C, Jamieson SSR, Carr JR, Leeson AA. 2020. Recent understanding of Antarctic supraglacial lakes using satellite remote sensing. Prog Phys Geogr. 44(6):837–869. https://doi.org/10.1177/0309133320916114
7. Arthur JF, Stokes CR, Jamieson SSR, Rachel Carr J, Leeson AA. 2020. Distribution and seasonal evolution of supraglacial lakes on Shackleton Ice Shelf, East Antarctica. Cryosphere. 14(11):4103–4120. https://doi.org/10.5194/tc-14-4103-2020
8. Arthur JF, Stokes CR, Jamieson SSR, Rachel Carr J, Leeson AA, Verjans V. 2022. Large interannual variability in supraglacial lakes around East Antarctica. Nat Commun. 13(1):1–12. https://doi.org/10.1038/s41467-022-29385-3
9. Banwell AF, Willis IC, Macdonald GJ, Goodsell B, Macayeal DR. Direct measurements of ice-shelf flexure caused by surface meltwater ponding and drainage. Nat Commun [Internet].(2019):1–10. https://doi.org/10.1038/s41467-019-08522-5
10. Barella R, Callegari M, Marin C, Klug C, Sailer R, Galos SP, Dinale R, Gianinetto M,

Notarnicola C. 2022. Combined Use of Sentinel-1 and Sentinel-2 for Glacier Mapping: An Application over Central East Alps. IEEE J Sel Top Appl Earth Obs Remote Sens. 15:4824–4834. https://doi.org/10.1109/JSTARS.2022.3179050

11. Baumhoer CA, Dietz AJ, Dech S, Kuenzer C. 2018. Remote Sensing of Antarctic Glacier and Ice-Shelf Front Dynamics — A Review. :1–28. https://doi.org/10.3390/rs10091445
12. Bell RE, Banwell AF, Trusel LD, Kingslake J. 2018. Antarctic surface hydrology and impacts on ice-sheet mass balance. Nat Clim Chang [Internet]. 8(12):1044–1052. https://doi.org/10.1038/s41558-018-0326-3
13. Bell RE, Chu W, Kingslake J, Das I, Tedesco M, Tinto KJ, Zappa CJ, Frezzotti M, Boghosian A, Lee WS. 2017. Antarctic ice shelf potentially stabilized by export of meltwater in surface river. Nature [Internet]. 544(7650):344–348. https://doi.org/10.1038/nature22048
14. Brogioni M, Andrews MJ, Urbini S, Jezek KC, Johnson JT, Leduc-Leballeur M, MacElloni G, Ackley SF, Bringer A, Brucker L, et al. 2023. Ice Sheet and Sea Ice Ultrawideband Microwave radiometric Airborne eXperiment (ISSIUMAX) in Antarctica: first results from Terra Nova Bay. Cryosphere. 17(1):255–278. https://doi.org/10.5194/tc-17-255-2023
15. Buzzard SC, Feltham DL, Flocco D. 2018. A Mathematical Model of Melt Lake Development on an Ice Shelf. J Adv Model Earth Syst. 10(2):262–283. https://doi.org/10.1002/2017MS001155
16. Cavalieri DJ, Parkinson CL. 2008. Antarctic sea ice variability and trends, 1979–2006. J Geophys Res. 113(C7):1–19. https://doi.org/10.1029/2007jc004564
17. Colosio P, Tedesco M, Ranzi R, Fettweis X. 2021. Surface melting over the Greenland ice sheet derived from enhanced resolution passive microwave brightness temperatures (1979-2019). Cryosphere. 15(6):2623–2646. https://doi.org/10.5194/tc-15-2623-2021
18. Cook AJ, Vaughan DG. 2010. Overview of areal changes of the ice shelves on the Antarctic Peninsula over the past 50 years. Cryosphere. 4(1):77–98. https://doi.org/10.5194/tc-4-77-2010
19. Dell R, Arnold N, Willis I, Banwell A, Williamson A, Pritchard H, Orr A. 2020. Lateral meltwater transfer across an Antarctic ice shelf. Cryosphere. 14(7):2313–2330. https://doi.org/10.5194/tc-14-2313-2020
20. Dell RL, Banwell AF, Willis IC, Arnold NS, Halberstadt ARW, Chudley TR, Pritchard HD. 2022. Erratum: Supervised classification of slush and ponded water on Antarctic ice

shelves using Landsat 8 imagery (Journal of Glaciology 68: 268 (401-414) DOI: 10.1017/jog.2021.114). J Glaciol. 68(268):415–416. https://doi.org/10.1017/jog.2022.15

21. Dirscherl M, Dietz AJ, Kneisel C, Kuenzer C. 2020. Automated mapping of antarctic supraglacial lakes using a machine learning approach. Remote Sens. 12(7). https://doi.org/10.3390/rs12071203
22. Fausto RS, Van As D, Ahlstrøm AP, Citterio M. 2012. Instruments and methods: Assessing the accuracy of Greenland ice sheet ice ablation measurements by pressure transducer. J Glaciol. 58(212):1144–1150. https://doi.org/10.3189/2012JoG12J075
23. Fricker HA, Arndt P, Brunt KM, Datta RT, Fair Z, Jasinski MF, Kingslake J, Magruder LA, Moussavi M, Pope A, et al. 2021. ICESat-2 Meltwater Depth Estimates: Application to Surface Melt on Amery Ice Shelf, East Antarctica. Geophys Res Lett. 48(8). https://doi.org/10.1029/2020GL090550
24. Friedl P. 2019. Derivation of glaciological parameters from time series of multi-mission remote sensing data - Applications to glaciers in Antarctica and the Karakoram (January).
25. Furfaro R, Picca P, Kargel JS, Science P. 2014. Global Land Ice Measurements from Space. Glob L Ice Meas from Sp.(July). https://doi.org/10.1007/978-3-540-79818-7
26. Gardner AS, Sharp MJ. 2010. A review of snow and ice albedo and the development of a new physically based broadband albedo parameterization. J Geophys Res Earth Surf. 115(1):1–15. https://doi.org/10.1029/2009JF001444
27. Geetha Priya M, Deva Jefflin AR, Luis AJ, Bahuguna IM. 2022. Estimation of surface melt induced melt pond depths over Amery Ice Shelf, East Antarctica using Multispectral and ICESat-2 data. Disaster Adv. 15(8):1–8. https://doi.org/10.25303/1508da01008
28. Ghiz ML, Scott RC, Vogelmann AM, Lenaerts JTM, Lazzara M, Lubin D. 2021. Energetics of surface melt in West Antarctica. Cryosphere. 15(7):3459–3494. https://doi.org/10.5194/tc-15-3459-2021
29. Halas P, Mouginot J, de Fleurian B, Langebroek PM. 2023. Impact of seasonal fluctuations of ice velocity on decadal trends observed in Southwest Greenland. Remote Sens Environ. 285(January). https://doi.org/10.1016/j.rse.2022.113419
30. Hall DK, Nghiem S V., Schaaf CB, DiGirolamo NE, Neumann G. 2009. Evaluation of surface and near-surface melt characteristics on the Greenland ice sheet using MODIS and QuikSCAT data. J Geophys Res Earth Surf. 114(4):1–13. https://doi.org/10.1029/2009JF001287

31. Hawes IAN, Safi K, Sorrell B, Webster-brown J, Arscott D. 2011. Summer-winter transitions in Antarctic ponds I : The physical environment Summer – winter transitions in Antarctic ponds I : The physical environment. (May). https://doi.org/10.1017/S0954102011000046
32. Horwath M, Dietrich R, Baessler M, Nixdorf U, Steinhage D, Fritzsche D, Damm V, Reitmayr G. 2006. Nivlisen, an Antarctic ice shelf in Dronning Maud Land: Geodetic-glaciological results from a combined analysis of ice thickness, ice surface height and ice-flow observations. J Glaciol. 52(176):17–30. https://doi.org/10.3189/172756506781828953
33. Husman SDR, Hu Z, Wouters B, Munneke PK, Veldhuijsen S, Lhermitte S . 2022. Remote Sensing of Surface Melt on Antarctica : Opportunities and Challenges. IEEE J Sel Top Appl Earth Obs Remote Sens. PP(Xxx):1–20vol. 16, pp. 2462-2480, 2023, doi: 10.1109/JSTARS.2022.3216953
34. Izeboud M, Lhermitte S. 2023. Remote Sensing of Environment Damage detection on antarctic ice shelves using the normalised radon transform. Remote Sens Environ [Internet]. 284(November 2022):113359. https://doi.org/10.1016/j.rse.2022.113359
35. Jakobs CL, Reijmer CH, van den Broeke MR, van de Berg WJ, van Wessem JM. 2021. Spatial Variability of the Snowmelt-Albedo Feedback in Antarctica. J Geophys Res Earth Surf. 126(2). https://doi.org/10.1029/2020JF005696
36. Jakobs CL, Reijmer CH, Smeets CJPP, Trusel LD, Van De Berg WJ, Van Den Broeke MR, Van Wessem JM. 2020. A benchmark dataset of in situ Antarctic surface melt rates and energy balance. J Glaciol. 66(256):291–302. https://doi.org/10.1017/jog.2020.6
37. Johnson A, Fahnestock M, Hock R. 2020. Evaluation of passive microwave melt detection methods on Antarctic Peninsula ice shelves using time series of Sentinel-1 SAR. Remote Sens Environ [Internet]. 250(February):112044. https://doi.org/10.1016/j.rse.2020.112044
38. Kaushik S, Cerino B, Trouve E, Karbou F, Yan Y, Ravanel L, Magnin F. 2022. Analysis of the Temporal Evolution of Ice Aprons in the Mont-Blanc Massif Using X and C-Band SAR Images. Front Remote Sens. 3(June):1–17. https://doi.org/10.3389/frsen.2022.930021
39. Kingslake J, Ely JC, Das I, Bell RE. 2017. Letter. Nat Publ Gr [Internet]. 544(7650):349–352. https://doi.org/10.1038/nature22049
40. Komac M, Holley R, Mahapatra P, van der Marel H, Bavec M. 2015. Coupling of GPS/GNSS and radar interferometric data for a 3D surface displacement monitoring of

landslides. Landslides. 12(2):241–257. https://doi.org/10.1007/s10346-014-0482-0

41. König M, Oppelt N. 2020. A linear model to derive melt pond depth on Arctic sea ice from hyperspectral data. Cryosphere. 14(8):2567–2579. https://doi.org/10.5194/tc-14-2567-2020
42. Konovalov Y V. 2021. Abatement of Ocean-Wave Impact by Crevasses in an Ice Shelf Abatement of Ocean-Wave Impact by Crevasses in an Ice Shelf. (January). https://doi.org/10.3390/jmse9010046
43. Lampkin DJ, Karmoskay CC. 2009. Surface melt magnitude retrieval over Ross Ice Shelf, Antarctica using coupled MODIS near-IR and thermal satellite measurements. Cryosph Discuss. 3(3):1069–1107. https://doi.org/10.5194/tcd-3-1069-2009
44. Mahagaonkar, A., Moholdt, G., and Schuler, T. V.: Recent Evolution of Supraglacial Lakes on ice shelves in Dronning Maud Land, East Antarctica, The Cryosphere Discuss. [preprint], https://doi.org/10.5194/tc-2023-4, in review, 2023.
45. Leitner JF, Perteneder F, Liu C, Rendl C, Haller M. 2013. Kolibri - Tiny and fast gestures for large pen-based surfaces. Conf Hum Factors Comput Syst - Proc.:1789–1798. https://doi.org/10.1145/2470654.2466236
46. Leppäranta M, Luttinen A, Arvola L. 2020. Physics and geochemistry of lakes in Vestfjella, Dronning Maud Land. Antarct Sci. 32(1):29–42. https://doi.org/10.1017/S0954102019000555
47. Liang D, Guo H, Zhang L, Cheng Y, Zhu Q, Liu X. 2021. Time-series snowmelt detection over the Antarctic using Sentinel-1 SAR images on Google Earth Engine. Remote Sens Environ. 256(February). https://doi.org/10.1016/j.rse.2021.112318
48. Lindbäck K, Moholdt G, Nicholls KW, Hattermann T, Pratap B, Thamban M, Matsuoka K. 2019. Spatial and temporal variations in basal melting at Nivlisen ice shelf, East Antarctica, derived from phase-sensitive radars. Cryosphere. 13(10):2579–2595. https://doi.org/10.5194/tc-13-2579-2019
49. Liu C, Hu R, Wang Y, Lin H, Zeng H, Wu D, Liu Z, Dai Y, Song X, Shao C. 2022. Monitoring water level and volume changes of lakes and reservoirs in the Yellow River Basin using ICESat-2 laser altimetry and Google Earth Engine. J Hydro-Environment Res [Internet]. 44(May):53–64. https://doi.org/10.1016/j.jher.2022.07.005
50. Liu H, Wang L, Jezek KC. 2006. Spatiotemporal variations of snowmelt in Antarctica derived from satellite scanning multichannel microwave radiometer and Special Sensor

Microwave Imager data (1978-2004). J Geophys Res Earth Surf. 111(1). https://doi.org/10.1029/2005JF000318

51. Lombardi D, Gorodetskaya I, Barruol G, Camelbeeck T. 2019. Thermally induced icequakes detected on blue ice areas of the East Antarctic ice sheet. Ann Glaciol. 60(79):45–56. https://doi.org/10.1017/aog.2019.26
52. Luis AJ, Alam M, Jawak SD. 2022. Spatiotemporal change analysis for snowmelt over the Antarctic ice shelves using scatterometers. (November):1–18. https://doi.org/10.3389/frsen.2022.953733
53. Lund J, Forster RR, Deeb EJ, Liston GE, Skiles SMK, Marshall HP. 2022. Interpreting Sentinel-1 SAR Backscatter Signals of Snowpack Surface Melt/Freeze, Warming, and Ripening, through Field Measurements and Physically-Based SnowModel. Remote Sens. 14(16). https://doi.org/10.3390/rs14164002
54. Manickam S, Bhattacharya A, Singh G, Yamaguchi Y. 2017. Estimation of Snow Surface Dielectric Constant from Polarimetric SAR Data. IEEE J Sel Top Appl Earth Obs Remote Sens. 10(1):211–218. https://doi.org/10.1109/JSTARS.2016.2588531
55. Masek JG, Wulder MA, Markham B, McCorkel J, Crawford CJ, Storey J, Jenstrom DT. 2020. Landsat 9: Empowering open science and applications through continuity. Remote Sens Environ. 248(October 2020). https://doi.org/10.1016/j.rse.2020.111968
56. Mortimer CA, Sharp M, Wouters B. 2016. Glacier surface temperatures in the Canadian High Arctic, 2000-15. J Glaciol. 62(235):963–975. https://doi.org/10.1017/jog.2016.80
57. Moussavi M, Pope A, Halberstadt ARW, Trusel LD, Cioffi L, Abdalat W. 2020. Antarctic supraglacial lake detection using landsat 8 and sentinel-2 imagery: Towards continental generation of lake volumes. Remote Sens. 12(1). https://doi.org/10.3390/RS12010134
58. Orr A, Deb P, Clem KR, Gilbert E, Bromwich DH, Boberg F, Colwell S, Hansen N, Lazzara MA, Mooney PA, et al. 2022. Characteristics of surface “melt potential” over Antarctic ice shelves based on regional atmospheric model simulations of summer air temperature extremes from 1979/80 to 2018/19. J Clim.:1–61. https://doi.org/10.1175/jcli-d-22-0386.1
59. Oza SR, Singh RKK, Vyas NK, Sarkar A. 2011. Study of inter-annual variations in surface melting over Amery Ice Shelf, East Antarctica, using space-borne scatterometer data. J Earth Syst Sci. 120(2):329–336. https://doi.org/10.1007/s12040-011-0055-8
60. Valerio L P, Shaw J, Gonzalez F, Robinson S, Kate J H. 2022. Contemporary Remote Sensing Tools for Integrated Assessment and Conservation Planning of Ice-free Antarctica.

(June):1–22.
61. Philpot WD. 1989. Bathymetric mapping with passive multispectral imagery. Appl Opt. 28(8):1569. https://doi.org/10.1364/ao.28.001569
62. Pina P, Vieira G. 2022. UAVs for Science in Antarctica. Remote Sens. 14(7):1–39. https://doi.org/10.3390/rs14071610
63. Pope A, Scambos TA, Moussavi M, Tedesco M, Willis M, Shean D, Grigsby S. 2016. Estimating supraglacial lake depth in West Greenland using Landsat 8 and comparison with other multispectral methods. Cryosphere. 10(1):15–27. https://doi.org/10.5194/tc-10-15-2016
64. Qiao G, Yuan X, Florinsky I, Popov S, He Y, Li H. 2023. Topography reconstruction and evolution analysis of outlet glacier using data from unmanned aerial vehicles in Antarctica. Int J Appl Earth Obs Geoinf [Internet]. 117(August 2022):103186. https://doi.org/10.1016/j.jag.2023.103186
65. Rakshita C, Sowjanya A, Swathi P, Geetha Priya M. 2023. Velocity Estimation of East Antarctic Glacier with SAR Offset Tracking---An Application of Image Processing. In: Smys S, Tavares JMRS, Shi F, editors. Comput Vis Bio-Inspired Comput. Singapore: Springer Nature Singapore; p. 323–331.
66. Rintoul SR. 2018. The global influence of localized dynamics in the Southern Ocean. Nature. 558(7709):209–218. https://doi.org/10.1038/s41586-018-0182-3
67. Safa F, Flouzat G. 1989. Speckle removal on radar imagery based on mathematical morphology. Signal Processing. 16(4):319–333. https://doi.org/10.1016/0165-1684(89)90029-7
68. Saunderson D, MacKintosh A, McCormack F, Jones RS, Picard G. 2022. Surface melt on the Shackleton Ice Shelf, East Antarctica (2003-2021). Cryosphere. 16(10):4553–4569. https://doi.org/10.5194/tc-16-4553-2022
69. Sergienko O V. 2022. No general stability conditions for marine ice-sheet grounding lines in the presence of feedbacks. Nat Commun. 13(1). https://doi.org/10.1038/s41467-022-29892-3
70. Sivalingam S, Murugesan GP, Dhulipala K, Kulkarni AV, Devaraj S. 2022. Temporal fluctuations of siachen glacier velocity: a repeat pass sar interferometry based approach. Geocarto Int. 37(17):4888–4910. https://doi.org/10.1080/10106049.2021.1899306
71. Sneed WA, Hamilton GS. 2007. Evolution of melt pond volume on the surface of the

Greenland Ice Sheet. Geophys Res Lett. 34(3):4–7. https://doi.org/10.1029/2006GL028697

72. Steiner N, Tedesco M. 2014. A wavelet melt detection algorithm applied to enhanced-resolution scatterometer data over Antarctica (2000-2009). Cryosphere. 8(1):25–40. https://doi.org/10.5194/tc-8-25-2014

73. Stevens LA, Behn MD, McGuire JJ, Das SB, Joughin I, Herring T, Shean DE, King MA. 2015. Greenland supraglacial lake drainages triggered by hydrologically induced basal slip. Nature. 522(7554):73–76. https://doi.org/10.1038/nature14480

74. Tovar-Sánchez A, Román A, Roque-Atienza D, Navarro G. 2021. Applications of unmanned aerial vehicles in Antarctic environmental research. Sci Rep [Internet]. 11(1):1–8. https://doi.org/10.1038/s41598-021-01228-z

75. Trusel LD, Frey KE, Das SB. 2012. Antarctic surface melting dynamics: Enhanced perspectives from radar scatterometer data. J Geophys Res Earth Surf. 117(2). https://doi.org/10.1029/2011JF002126

76. Trusel LD, Pan Z, Moussavi M. 2022. Repeated Tidally Induced Hydrofracture of a Supraglacial Lake at the Amery Ice Shelf Grounding Zone. Geophys Res Lett. 49(7):1–11. https://doi.org/10.1029/2021GL095661

77. Tuckett PA, Ely JC, Sole AJ, Lea JM, Livingstone SJ, Jones JM, Van Wessem JM. 2021. Automated mapping of the seasonal evolution of surface meltwater and its links to climate on the Amery Ice Shelf, Antarctica. Cryosphere. 15(12):5785–5804. https://doi.org/10.5194/tc-15-5785-2021

78. Tuckett PA, Ely JC, Sole AJ, Livingstone SJ, Davison BJ, Melchior van Wessem J, Howard J. 2019. Rapid accelerations of Antarctic Peninsula outlet glaciers driven by surface melt. Nat Commun [Internet]. 10(1). https://doi.org/10.1038/s41467-019-12039-2

79. Vaňková I, Cook S, Winberry JP, Nicholls KW, Galton-Fenzi BK. 2021. Deriving Melt Rates at a Complex Ice Shelf Base Using In Situ Radar: Application to Totten Ice Shelf. Geophys Res Lett. 48(7). https://doi.org/10.1029/2021GL092692

80. Yuan X, Qiao G, Li Y, Li H, Xu R. 2020. Modelling of glacier and ice sheet micro-topography based on unmanned aerial vehicle data, Antarctica. Int Arch Photogramm Remote Sens Spat Inf Sci - ISPRS Arch. 43(B3):919–923. https://doi.org/10.5194/isprs-archives-XLIII-B3-2020-919-2020

81. Zhu J, Tan S, Tsang L, Kang DH, Kim E. 2021. Snow Water Equivalent Retrieval Using

Active and Passive Microwave Observations. Water Resour Res. 57(7):1–21. https://doi.org/10.1029/2020WR027563

82. Zhu Q, Guo H, Zhang L, Liang D, Liu X, Zhou H. 2023. High-resolution spatio-temporal analysis of snowmelt over Antarctic Peninsula ice shelves from 2015 to 2021 using SAR images High-resolution spatio-temporal analysis of snowmelt over Antarctic Peninsula ice shelves from 2015 to 2021 using SAR images. (March). https://doi.org/10.1080/17538947.2023.2181991